Stability and dynamics of a chemotaxis system with deformed free-surface in a shallow chamber

Symphony Chakraborty, Filip Ivancic, Maxim Solovchuk, and Tony Wen-Hann Sheu

Stability and dynamics of a chemotaxis system with deformed free-surface in a shallow chamber

Symphony Chakraborty,[1] Filip Ivancic,[2] Maxim Solovchuk,[2,3] and Tony Wen-Hann Sheu[1,2,a)]

[1]*Center for Advanced Study in Theoretical Sciences, National Taiwan University, No. 1, Sec. 4, Roosevelt Road, Taipei 10617, Taiwan*
[2]*Department of Engineering Science and Ocean Engineering, National Taiwan University, No. 1, Sec. 4, Roosevelt Road, Taipei 10617, Taiwan*
[3]*Institute of Biomedical Engineering and Nanomedicine, National Health Research Institute, No. 35, Keyan Road, Zhunan 35053, Taiwan*

Complex bioconvection patterns have been studied analytically, experimentally, and numerically previously only for a flat free-surface of a suspension of chemotaxis bacteria in a shallow/deep chamber. In this paper, we have considered a two-dimensional chemotaxis-diffusion-convection system with a deformed free-surface. The influence of aggregation of chemotactic cells on the deformed free-surface of a shallow chamber is studied analytically. The aim of this paper is to investigate the nature of the instability in the chemotaxis-diffusion-convection system. We performed a detailed linear stability analysis of a steady-state cell and oxygen concentration distribution. The system becomes dominated by nonlinear convection terms beyond a critical Rayleigh number Ra_τ, which also depends on the critical wavenumber k as well as the other parameters. We have investigated that how the critical Rayleigh number in this system varies with three different sets of parameters. A weakly nonlinear analysis is carried out as well to determine the relative stability of the pattern formation at the onset of instability. A reactance between rolls, squares, hexagons, and mixed mode pattern is investigated in detail. Further research should link the weakly nonlinear analysis with the bifurcation analysis. Some important direct numerical simulation results have been presented in the support of linear stability analysis. Comparison of the analytical steady-state solution shows good agreement with the numerical result. *Published by AIP Publishing.* https://doi.org/10.1063/1.5038613

NOMENCLATURE

c	Concentration of oxygen (mol)
c_{air}	Concentration of oxygen in air (mol)
D	Diffusivity of the bacterium (m^2 s^{-1})
$\varepsilon(\equiv h_0/L)$	Aspect ratio
h_0	Container height (m)
H	Chemotaxis head
$\mathbf{j}$	Vertical unit vector upwards
L	Length of the container (m)
Le	Lewis number
n	Density number of bacteria (m^{-3})
$\mathbf{n}$	Unit outward normal vector
n_0	Initial density number of bacteria (m^{-3})
$\bar{n}_0$	Initial density number of bacteria (m^{-3})
p	Pressure (kg m s^{-2})
Pr	Prandtl number
Ra	Rayleigh number
S	Dimensionless chemotaxis sensitivity
S_{dim}	Dimensional chemotaxis sensitivity (m^5 s^{-1} mol^{-1})
t	Time (s)
$\mathbf{u} = (u, v)$	Velocity vector (m s^{-1})
V_b	Volume of the bacterium (m^3)
$\mathbf{x} = (x, y)$	Coordinate axes (m)

Greek symbols

κ	Bacterium oxygen consumption rate (s^{-1})
μ	Dynamic viscosity (kg m^{-1} s^{-1})
ν	Kinematic viscosity (m^2 s^{-1})
ρ	Fluid density (kg m^{-3})
ρ_b	Bacterium volumetric mass density (kg m^{-3})

Subscripts

$\cdot_b$	Bacterium
$\cdot_O$	Oxygen
$\cdot_\tau$	Taxis

I. INTRODUCTION

In the last few decades, many research groups have been motivated to do a lot of studies experimentally, theoretically, and numerically with the objective to understand the dynamics of the pattern formation or emerging phenomena in suspensions of bacterial motility due to its significant role in medical, industrial, and geophysical areas. The phenomenon is known as bioconvection. Bioconvection and different mechanisms of up-swimming micro-organisms have been reviewed.[1] Many organisms or insects are interacted through the process of chemotaxis. Moreover, chemotaxis-diffusion-convection has been successfully illustrated by experiments[2,3] and numerical simulations[4,5] on suspensions of bacteria contained in a

---

a)Author to whom correspondence should be addressed: twhsheu@ntu.edu.tw

water container. Initially, in a stirred container, the oxygen and cell concentrations are equal. Bacteria consume oxygen, and the oxygen concentration starts to fall everywhere accordingly except at the free-surface which is exposed to air, thereby creating a vertical concentration difference. Bacteria begin to move up to a higher concentration level of oxygen and accumulate close to the air-water interface. Afterward buoyancy induced instability appears near the interface. Then the bacteria start to fall into a fluid in the form of plumes due to buoyancy instability.

A chemotaxis-diffusion-convection mathematical model has been previously introduced.[3,5,6] Most of the theoretical, experimental, and numerical studies have been focused on the pattern formation of micro-organisms and blow-up phenomena in finite time either for a flat free-surface or the case that both top and bottom surfaces are rigid. Avramenko and Kuznetsov[7] performed a linear stability analysis to obtain a correlation between the critical value of the bioconvection Rayleigh number and the traditional, "thermal" Rayleigh number by heating from below and compared for the rigid top surface and open flat free-surface, whereas Kuznetsov[8] compared the same for inclined temperature gradient. Their results proved that heating from below makes the system more unstable and helps the development of bioconvection.

Formation and stability of plumes result from the balance between chemotaxis, diffusion, and convection of bacteria. So far the stability analyses of the chemotaxis system were performed for the flat free-surface where chemotaxis is known to bring instability to a nonlinear system and leads to aggregation.[1–3,7–11] Kowalczyk *et al.*[12] performed a detailed study of linear stability analysis of two different models on a homogeneous cell solution with the aim of checking their potential for plume formation. The linear stability analysis of the chemotaxis-diffusion-convection system showed that a condition for linear instability depends on the taxis Rayleigh number Ra_τ.[3] Metcalfe and Pedley[13] and Ma *et al.*[14] performed a weakly nonlinear stability analysis to investigate the stability of different patterns formed by the chemotaxis system. The hydrodynamic vortices formed by convection strengthen the circulation of fluid and enhance the intake of oxygen into the solvent.[15] Duan *et al.*[16] proved the global existence of the chemotaxis-Stokes system for a small initial bacterial population density, whereas Liu and Lorz[17] proved for a large initial bacterial population density as well as global existence of 3D weak solutions for the chemotaxis-Stokes equations. Chertock *et al.*[4] numerically studied the plume formation and merging for the flat free-surface, whereas the number and the shape of the plumes can be controlled by the initial bacterial population density. Chertock *et al.*[4] also revealed the convergence toward numerically stable stationary plumes for low and high initial cell densities.

Stability of cell pattern formation would be crucial to study in this type of chemotaxis system. However, some cell patterns were mentioned in the work of Chandrasekhar,[18] while other cell patterns were redundantly discussed in the work of Bestehorn.[19] In bioconvection mainly three types of patterns have been found such as rolls, rectangular/squares, and hexagons. Buzano and Golubitsky[20] and Golubitsky

et al.[21] have found two types of hexagon, namely, up- and down-hexagon. The up-hexagons are those which appear in the flows up in the center and down at the edges. Those which appear in the flows down in the center and up at the edges are known as down-hexagons. They have simplified all the calculations by considering both the patterns which fit on the hexagonal lattice (rolls and hexagons) or those which fit on a square lattice (rolls and squares). Their techniques made easy to study the cell patterns. The relative stability of hexagons and squares is not possible to compare since they do not fit on the same lattice. The symmetries of the system restrict the possible solutions. Possibly one or more patterns may be stabilized at a finite amplitude. Commonly hexagons are stabilized at the lower value of the Rayleigh number than the rolls. The other types of patterns may be stable near the bifurcation point in up-down symmetric systems. The triangular type of cell pattern is also mentioned by Chandrasekhar[18] which can be considered, equally, as hexagonal.

The novelty of the present study is that the deformed free-surface of the chemotaxis instability in the system is considered for the first time to explore the linear and nonlinear dynamics and stability of the system. Most of the previously published studies have been devoted to the chemotactic system with the flat free-surface and have successfully explained the formation of patterns. However, the free-surface is normally deformable in natural conditions. It would be more interesting to study the formation of patterns on the deformed free-surface. However, it was predicted previously that the chemotaxis system is unstable in the inclined domain. To the best of the authors' knowledge, the stability analysis of the chemotaxis-diffusion-convection system for the deformed free-surface has not been performed yet. But it may be crucial to study as it has geophysical applications.

The paper is organized as follows. The mathematical formulation of the chemotaxis-convection-diffusion system is presented in Sec. II. The linear stability analysis of the steady-state solution, the analytical solution for shallow chambers, and stability results have been discussed in Sec. III. Weakly nonlinear stability analysis of the problem and reactance between different patterns have been illustrated in Sec. IV. Bifurcation to different patterns has been discussed in Sec. V. In Sec. VI, some important numerical simulation results have been shown and discussed. Finally, some conclusions are summarized in Sec. VII.

II. MATHEMATICAL MODEL

A two-dimensional shallow water chamber with the deformed free-surface is considered. A Cartesian coordinate system (x, y) is used, with the x-axis along the stream-wise direction and the y-axis pointing vertically upwards. The top of the chamber is open to the air, and the motion of the fluid in a rectangular chamber satisfies the tangential stress condition prescribed on the free-surface. The bottom and the side walls are rigid and impermeable to bacteria and oxygen (see Fig. 1).

The dimensional form of governing equations for the chemotaxis-diffusion-convection system in an incompressible viscous fluid is as follows:
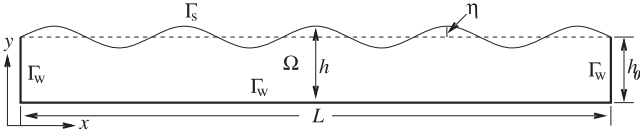
FIG. 1. A schematic diagram of a two-dimensional chemotaxis system with the liquid-air interface Γ_s, where the oxygen concentration is equal to that of air, not crossed by bacteria. A no-slip boundary condition is imposed at the container walls Γ_w.

$$\nabla \cdot \mathbf{u} = 0, \tag{1a}$$

$$\rho(\mathbf{u}_t + \mathbf{u} \cdot \nabla \mathbf{u}) + \nabla p - \mu\nabla^2\mathbf{u} = -nV_b g(\rho_b - \rho)\mathbf{j}, \tag{1b}$$

$$n_t + \nabla \cdot [\mathbf{u}n - D_b\nabla n + S_{dim}r(c)n\nabla c] = 0, \tag{1c}$$

$$c_t + \nabla \cdot (\mathbf{u}c - D_O\nabla c) = -n\kappa r(c). \tag{1d}$$

In the above equations, $\mathbf{u} = (u, v)$ denotes the fluid velocity in the (x, y)-direction, p is the hydrostatic pressure, ρ and μ are the fluid density and viscosity, respectively, n is the number of bacteria per unit area, V_b and ρ_b are the volume and volumetric mass density of a cell, respectively, c is the oxygen concentration, $V_b g(\rho_b - \rho)\mathbf{j}$ is the buoyancy force exerted by a cell on the liquid in the vertical direction, $\mathbf{j}$ is the unit vector, S_{dim} is the dimensional chemotaxis sensitivity, D_b and D_O are the cell and oxygen diffusivities, κ is the rate of oxygen consumption by a bacterium, and $r(c)$ is the non-dimensional cut-off function for oxygen concentration. The cut-off function $r(c)$ is defined by the step function

$$r(c) = \begin{cases} 1, & if \quad c > c^* \\ 0, & if \quad c \leqslant c^* \end{cases}, \tag{2}$$

where $c^* = 0.3$.

Bacteria are slightly denser than water, such that $\rho_b > \rho$, where bacteria are supposed to swim in the water during the consumption of oxygen. As a result, we have considered $(\rho_b - \rho)/\rho \ll 1$ and $nV_b \ll 1$, respectively. The oxygen consumption is proportional to the cell population density n. Both bacteria (n) and oxygen (c) are advected by the liquid. When the concentration of oxygen is higher than a threshold, the cell becomes stable; i.e., cells neither consume oxygen nor swim toward the higher oxygen concentration region.

The set of Eqs. (1a)–(1d) is closed with the boundary conditions and will be solved in a two-dimensional rectangular container (Ω). The dynamic and kinematic boundary conditions at the interface ($y = h(x, t)$) are

$$\mathbf{n} \cdot \tau \cdot \mathbf{n} = 0, \quad \mathbf{t} \cdot \tau \cdot \mathbf{n} = 0, \quad S_{dim}nr(c)\nabla c \cdot \mathbf{n} = D_b\nabla n \cdot \mathbf{n},$$
$$c = c_{air}, \tag{3a}$$

$$h_t = v - uh_x, \tag{3b}$$

where τ is the stress tensor for the liquid, $\mathbf{n}\left(= \frac{(-h_x, 1)}{N} \right)$ and $\mathbf{t}\left(= \frac{(1, h_x)}{N} \right)$ are the unit outward normal and tangential vectors on the interface, and $N = \sqrt{1 + h_x^2}$. A no-slip boundary condition is applied on the container walls (Γ_w); the fluxes of bacteria and oxygen are equal to zero,

$$u = 0, \quad v = 0, \quad \nabla n \cdot \mathbf{n} = 0, \quad \nabla c \cdot \mathbf{n} = 0. \tag{3c}$$

The characteristic bacterial density is defined as the average of the initial bacterial population

$$\bar{n}_0 = \frac{1}{|\Omega|} \int_\Omega n_0(x, t)dx. \tag{4}$$

By the choice of this characteristic bacterial density, the total number of bacteria can be measured easily in each simulation for different initial distributions of bacteria.

Equations (1)–(3) can be expressed in terms of their dimensionless forms by using the following variables:

$$x = Lx', \quad y = h_0y', \quad h = h_0h', \quad n = \bar{n}_0n', \quad c = c_{air}c',$$
$$t = \frac{h_0^2}{\varepsilon D_b}t', \quad p = \frac{\mu D_b}{\varepsilon h_0^2}p', \quad u = \frac{D_b}{h_0}u', \quad v = \frac{\varepsilon D_b}{h_0}v', \tag{5}$$

where h_0 and L are the characteristic length scales in the horizontal and vertical direction, respectively. $\varepsilon = \frac{h_0}{L} \ll 1$ is an aspect ratio. Finally, after dropping the prime from the dimensionless quantities, the dimensionless Navier-Stokes equations for the incompressible fluid flow along with the Keller-Segel equation can be read as

$$\frac{\partial u}{\partial x} + \frac{\partial v}{\partial y} = 0, \tag{6a}$$

$$\varepsilon\left(\frac{\partial u}{\partial t} + u\frac{\partial u}{\partial x} + v\frac{\partial u}{\partial y}\right) + Pr_\tau\frac{\partial p}{\partial x} = Pr_\tau\left(\varepsilon^2\frac{\partial^2 u}{\partial x^2} + \frac{\partial^2 u}{\partial y^2}\right), \tag{6b}$$

$$\varepsilon^3\left(\frac{\partial v}{\partial t} + u\frac{\partial v}{\partial x} + v\frac{\partial v}{\partial y}\right) + Pr_\tau\frac{\partial p}{\partial y} = \varepsilon^2 Pr_\tau\left(\varepsilon^2\frac{\partial^2 v}{\partial x^2} + \frac{\partial^2 v}{\partial y^2}\right)$$
$$- \varepsilon Pr_\tau Ra_\tau n, \tag{6c}$$

$$\varepsilon\left(\frac{\partial n}{\partial t} + u\frac{\partial n}{\partial x} + v\frac{\partial n}{\partial y}\right) - \left(\varepsilon^2\frac{\partial^2 n}{\partial x^2} + \frac{\partial^2 n}{\partial y^2}\right)$$
$$= -Sr(c)n\left(\varepsilon^2\frac{\partial^2 c}{\partial x^2} + \frac{\partial^2 c}{\partial y^2}\right) - Sr(c)\left(\varepsilon^2\frac{\partial c}{\partial x}\frac{\partial n}{\partial x} + \frac{\partial c}{\partial y}\frac{\partial n}{\partial y}\right), \tag{6d}$$

$$\varepsilon\left(\frac{\partial c}{\partial t} + u\frac{\partial c}{\partial x} + v\frac{\partial c}{\partial y}\right) = Le_\tau\left(\varepsilon^2\frac{\partial^2 c}{\partial x^2} + \frac{\partial^2 c}{\partial y^2}\right) - Hr(c)n. \tag{6e}$$

The dimensionless parameters are defined as

$$Pr_\tau = \frac{\nu}{D_b}, \quad Ra_\tau = \frac{gV_b\bar{n}_0(\rho_b - \rho)h_0^3}{D_b\mu}, \quad S = \frac{S_{dim}c_{air}}{D_b},$$
$$H = \frac{\kappa\bar{n}_0h_0^2}{c_{air}D_b}, \quad Le_\tau = \frac{D_O}{D_b}, \tag{7}$$

where Pr_τ is the taxis Prandtl number, Ra_τ is the taxis Rayleigh number (buoyancy-driven flow), Le_τ is the taxis Lewis number, S is the dimensionless chemotaxis sensitivity, and H is the chemotaxis head. The chemotaxis head represents the consumption of the chemo-attractant by the cell. The chemotaxis system is characterized by the chemotaxis sensitivity (S) and head (H). It can be seen from Eq. (7) that only Ra_τ and H depend on the characteristic length L and the characteristic bacterial density $\bar{n}_0$. The hydrodynamic and chemotaxis transport equations are characterized by the above mentioned five non-dimensional parameters. Ra_τ serves as the nonlinear control parameter of the chemotaxis-diffusion-convection system.

The above set of dimensionless governing equations is subjected to the dimensionless boundary conditions prescribed on the deformed free-surface $y = h(x, t)$,

$$-p + 2\varepsilon^2\left[\varepsilon^2\frac{\partial u}{\partial x}\left(\frac{\partial h}{\partial x}\right)^2 + \frac{\partial v}{\partial y} + \left(\frac{\partial u}{\partial y} + \varepsilon^2\frac{\partial v}{\partial x}\right)\frac{\partial h}{\partial x}\right] = 0, \quad (8a)$$

$$\left(\frac{\partial u}{\partial y} + \varepsilon^2\frac{\partial v}{\partial x}\right)\left(1 - \varepsilon^2\left(\frac{\partial h}{\partial x}\right)^2\right) + 2\varepsilon^2\left(\frac{\partial u}{\partial x} - \frac{\partial v}{\partial y}\right)\frac{\partial h}{\partial x} = 0, \quad (8b)$$

$$Sr(c)n\left(\frac{\partial c}{\partial y} - \varepsilon^2\frac{\partial c}{\partial x}\frac{\partial h}{\partial x}\right) - \frac{\partial n}{\partial y} + \varepsilon^2\frac{\partial n}{\partial x}\frac{\partial h}{\partial x} = 0, \quad (8c)$$

$$c = 1, \quad (8d)$$

and on the other boundaries,

$$u = 0, \quad v = 0, \quad \frac{\partial n}{\partial y} - \varepsilon^2\frac{\partial n}{\partial x}\frac{\partial h}{\partial x} = 0, \quad \frac{\partial c}{\partial y} - \varepsilon^2\frac{\partial c}{\partial x}\frac{\partial h}{\partial x} = 0. \quad (8e)$$

The kinematic boundary condition is

$$\frac{\partial h}{\partial t} = v - u\frac{\partial h}{\partial x}. \quad (8f)$$

III. LINEAR STABILITY ANALYSIS

A. Steady-state solutions

In the steady-state flow, the fluid properties of the system do not change over time. Pressure, velocity, cell, and oxygen concentrations will change in the y-direction only. The solution for $p(y)$ is obtained as follows by integrating Eq. (6c) with the boundary condition (8a):

$$p(y) = \varepsilon Ra_\tau(1 - y). \quad (9)$$

The solutions for $n(y)$ and $c(y)$ will be obtained from Eqs. (6d) and (6e),

$$S\nabla \cdot (r(c)n\nabla c) = \nabla^2 n, \quad (10a)$$

$$Le_\tau\nabla^2 c - Hnr(c) = 0. \quad (10b)$$

It is clear from Eq. (2) that if the cut-off function for oxygen concentration $r(c)$ is zero, then there will be no motion of bacteria in the domain, whereas the presence of the oxygen concentration, i.e., $r(c) = 1$ in the entire domain, activates the bacteria. Let us set $n(y) = n(x, y)$ and $c(y) = c(x, y)$ (independent of x). Then, from Eq. (10), we obtain

$$S\left[nc_y\right]_y = n_{yy}, \quad (11a)$$

$$Le_\tau c_{yy} = Hn. \quad (11b)$$

The procedure of integrating Eq. (11) and recalling the boundary conditions yields first

$$Snc_y = n_y \quad (12a)$$

and

$$c_y(1) = \int_0^1 n\,dy. \quad (12b)$$

Second, using Eq. (11), we obtain

$$Le_\tau c_{yyy} = Hn_y = HSnc_y = SLe_\tau c_{yy}c_y. \quad (13)$$

Finally, the following ordinary differential equation can be derived as

$$c_{yy} = \frac{S}{2}\left((c_y)^2 + A^*\right), \quad (14)$$

where A^* is a constant. From Eq. (12a), we would get the steady solution as

$$c(y) = 1 - \frac{2}{S}\ln\left(\frac{\cos\left(\frac{S}{2}A^*y\right)}{\cos\left(\frac{S}{2}A^*\right)}\right), \quad (15a)$$

$$n(y) = \frac{S}{2}\frac{Le_\tau A^{*2}}{H}\sec^2\left(\frac{S}{2}A^*y\right), \quad (15b)$$

where the constant A^* is determined from the transcendental equation,[3]

$$\tan\left(\frac{S}{2}A^*\right) = \frac{H}{Le_\tau}\frac{1}{A^*}. \quad (16)$$

Expanding the above equation yields the value of A^* in the order of $O(H/Le_\tau)$. After substituting the value of A^* into Eq. (15), we will get the steady-state concentrations of cell and oxygen. The expansion of Eq. (16) is only possible when $A^*\tan\left(\frac{S}{2}A^*\right) = \frac{H}{Le_\tau} \ll 1$. It is necessary to expand the steady state solutions (15) and (16) in powers of H/Le_τ. The expansion for A^* in Eq. (16) can be read as

$$A^* = \left(\frac{2H}{SLe_\tau}\right)^{1/2}\left(1 - \frac{S}{12}\frac{H}{Le_\tau} + \frac{7S^2}{288}\frac{H^2}{Le_\tau^2} + O\left(\frac{H}{Le_\tau}\right)^3\right). \quad (17)$$

Then Eq. (15b) gives

$$n = 1 + \frac{S}{6}\left(3y^2 - 1\right)\frac{H}{Le_\tau} + \frac{S^2}{18}\left(1 - 3y^2 + 3y^4\right)\frac{H^2}{Le_\tau^2} + O\left(\frac{H}{Le_\tau}\right)^3. \quad (18)$$

Similarly, the oxygen concentration at the steady-state, which also appears in the governing equations, is given by

$$c = 1 + \frac{1}{2}\left(y^2 - 1\right)\frac{H}{Le_\tau} + \frac{S}{24}\left(y^2 - 1\right)^2\frac{H^2}{Le_\tau^2} + O\left(\frac{H}{Le_\tau}\right)^3. \quad (19)$$

It would be noteworthy to mention here that this shallow chamber instability problem depends on H and Le_τ and $Le_\tau \gg H$. It is also noticed from Eqs. (17)–(19) that $c(y)$ and $n(y)$ can be written as a function of two variables y and SH/Le_τ. In general, the above system of governing equations (21) and (22) cannot be solved analytically, but it has been possible to find an analytical expression only for a very shallow chamber, i.e., $\frac{H}{Le_\tau}\frac{1}{A^*} \ll 1$.

The aim of linear stability analysis is to investigate the onset of the buoyancy-driven instability. The instability starts to exist if the Rayleigh number, which is the ratio of buoyancy and viscous forces, reaches a certain critical value. In this section, we seek to obtain the critical Rayleigh number which is a function of the physical parameters of the system. We first linearize the governing equations in Eq. (6) for small perturbations from the steady-state. Then, the resulting equations are solved for perturbations with a wavenumber k which corresponds to the dimensionless wavelength $\lambda = 2\pi/k$. Finally, we shall calculate the corresponding temporal growth rate σ (which is a complex). We thus perturb the basic state and introduce a stream function ψ. The velocity components u and

v can be written as $u = \psi_y$ and $v = -\psi_x$. Then, we proceed to perform decomposition on normal modes,

$$u(\mathbf{x}, t) = \Re\left(\psi'(y)e^{(ikx+\sigma t)}\right), \tag{20a}$$

$$v(\mathbf{x}, t) = \Re\left(-ik\psi(y)e^{(ikx+\sigma t)}\right), \tag{20b}$$

$$p(\mathbf{x}, t) = p(y) + \Re\left(P(y)e^{(ikx+\sigma t)}\right), \tag{20c}$$

$$n(\mathbf{x}, t) = n(y) + \Re\left(N(y)e^{(ikx+\sigma t)}\right), \tag{20d}$$

$$c(\mathbf{x}, t) = c(y) + \Re\left(C(y)e^{(ikx+\sigma t)}\right), \tag{20e}$$

$$h(x, t) = 1 + \Re\left(\eta e^{(ikx+\sigma t)}\right), \tag{20f}$$

where $\Re$ stands for the real value of the complex part and $\mathbf{x} = (x, y)$. Thus, we obtain

$$\left[\frac{d^2}{dy^2} - \left(\frac{\varepsilon\sigma}{Pr_\tau} + \varepsilon^2 k^2\right)\right]\left(\frac{d^2}{dy^2} - \varepsilon^2 k^2\right)\psi + i\varepsilon k Ra_\tau N = 0, \tag{21a}$$

$$\frac{d^2 N}{dy^2} - Sr(c)\frac{dc}{dy}\frac{dN}{dy} - \left[\varepsilon\sigma + \varepsilon^2 k^2 + Sr(c)\left(\frac{d^2 c}{dy^2} + r(c)n\frac{H}{Le_\tau}\right)\right]N$$

$$= Sr(c)\left(\frac{dn}{dy}\frac{dC}{dy} + \frac{\varepsilon n\sigma}{Le_\tau}C\right) - i\varepsilon k\psi\left(\frac{dn}{dy} + r(c)n\frac{S}{Le_\tau}\frac{dc}{dy}\right), \tag{21b}$$

$$\frac{d^2 C}{dy^2} - \left(\frac{\varepsilon\sigma}{Le_\tau} + \varepsilon^2 k^2\right)C + i\frac{\varepsilon k}{Le_\tau}\frac{dc}{dy}\psi - \frac{H}{Le_\tau}r(c)N = 0. \tag{21c}$$

The solutions of the above system of equations (21) are sought-out subject to the boundary conditions prescribed at the interface and at the other boundaries,

$$\frac{d^3\psi(1)}{dy^3} - \left(\frac{\varepsilon\sigma}{Pr_\tau} + 3\varepsilon^2 k^2\right)\frac{d\psi(1)}{dy} + \frac{k^2}{\sigma}\frac{dp(1)}{dy}\psi(1) = 0, \tag{22a}$$

$$\frac{d^2\psi(1)}{dy^2} + \varepsilon^2 k^2\psi(1) = 0, \tag{22b}$$

$$Sr(c)\left[N(1)\frac{dc(1)}{dy} + n(1)\frac{dC(1)}{dy}\right.$$

$$\left. - \frac{ik}{\sigma}\left(\frac{dc(1)}{dy}\frac{dn(1)}{dy} + n(1)\frac{d^2 c(1)}{dy^2}\right)\right]$$

$$= \frac{ik}{\sigma}\frac{d^2 n(1)}{dy^2}\psi(1) + \frac{dN(1)}{dy}, \tag{22c}$$

$$C(1) - i\frac{k}{\sigma}\frac{dc(1)}{dy}\psi(1) = 0, \tag{22d}$$

$$\psi(0) = \frac{d\psi(0)}{dy} = 0, \tag{22e}$$

$$\frac{dN(0)}{dy} = \frac{dC(0)}{dy} = 0. \tag{22f}$$

It is noteworthy to mention that the instability problem for shallow chambers depends on the parameters S, H, and Le_τ. The above governing equations (21) where all the coefficients are functions of y and can only be solved for shallow chambers analytically.

B. Analytical solutions for shallow chambers

We would like to express C, N, and ψ as a series in powers of $\frac{SH}{Le_\tau}$. Then the leading term (and higher orders if desired) will be possible to obtain in each of the series. For the sake of simplicity, we have considered the case with small wavenumber $k \sim \frac{SH}{Le_\tau}$ such that $k = \tilde{k}\frac{SH}{Le_\tau}$ is of order $O(1)$ (this is to keep the dimensional wavenumber to be fixed as $h \to 0$). Both the higher-order derivative and the right-hand side must hold in Eq. (21a) at the leading order of ψ, which is the required condition to get a non-trivial solution. Then, the reduced equation will take the form

$$\left(\frac{d^2}{dy^2} - \frac{\varepsilon\sigma}{Pr_\tau}\right)\frac{d^2\psi}{dy^2} = -i\varepsilon\tilde{k}\frac{SH}{Le_\tau}N Ra_\tau, \tag{23}$$

i.e., the viscous force, $\frac{d^4\psi}{dy^4}$, balances the buoyancy force on the right-hand side, leaving aside the time dependence σ. Without any loss of generality, we have also specified that $N = 1$ at $y = 1$ and set $C = \frac{H}{Le_\tau}\bar{C}$. Now, we have the possibility of getting leading-orders of $\bar{C}$ and N in Eqs. (21b) and (21c), which prospectively lead to the non-trivial solutions, as follows:
Case I:

$$Ra_\tau \sim O(1), \quad \sigma \sim O\left(\frac{SH}{Le_\tau}\right), \quad \frac{d^2\bar{C}}{dy^2} = N, \quad \frac{d^2 N}{dy^2} = 0.$$

Case II:

$$Ra_\tau \sim O\left(\frac{Le_\tau}{SH}\right), \quad \sigma \sim O\left(\frac{SH}{Le_\tau}\right), \quad \frac{d^2\bar{C}}{dy^2} = N, \quad \frac{d^2 N}{dy^2} = 0.$$

It turns out that case I leads to negative values of σ, i.e., stability, in all circumstances. Here, we perform the analysis only for case II.

Now, we seek expansions of the form

$$N(y) = \sum_{i=0}^{\infty} N_i(y)\left(\frac{SH}{Le_\tau}\right)^i, \quad \bar{C}(y) = \sum_{i=0}^{\infty} \bar{C}_i(y)\left(\frac{SH}{Le_\tau}\right)^i,$$

$$\psi(y) = \sum_{i=0}^{\infty} \psi_i(y)\left(\frac{SH}{Le_\tau}\right)^i,$$

and

$$\sigma(\tilde{k}) = \sum_{i=1}^{\infty} \sigma_i(\tilde{k})\left(\frac{SH}{Le_\tau}\right)^i, \quad Ra_\tau(\tilde{k}) = \sum_{i=-1}^{\infty} Ra_{\tau_i}(\tilde{k})\left(\frac{SH}{Le_\tau}\right)^i. \tag{24}$$

So, at the leading order, the governing equations become

$$\frac{d^4\psi_0}{dy^4} = -i\varepsilon\tilde{k}N_0 Ra_{\tau-1}, \quad \frac{d^2\bar{C}_0}{dy^2} = N_0, \quad \frac{d^2 N_0}{dy^2} = 0, \tag{25}$$

with the boundary conditions

$$\frac{d^3\psi_0(1)}{dy^3} = 0, \quad \frac{d^2\psi_0(1)}{dy^2} = 0, \quad \bar{C}_0(1) = 0, \quad \frac{dN_0(1)}{dy} = 0,$$

$$\frac{d\psi_0(0)}{dy} = 0, \quad \psi_0(0) = 0, \quad \frac{dN_0(0)}{dy} = 0, \quad \frac{d\bar{C}_0(0)}{dy} = 0. \tag{26}$$

In this study, we have arbitrarily set $N_0 = 1$ at $y = 1$ and the corresponding solutions are

$$\psi_0(y) = -\frac{i\tilde{k}\varepsilon Ra_{\tau_{-1}}}{24} y^2 (y^2 - 4y + 6), \tag{27a}$$

$$\bar{C}_0(y) = \frac{1}{2}(y^2 - 1), \tag{27b}$$

$$N_0(y) = 1. \tag{27c}$$

At the next order, the governing equations are

$$\frac{d^4\psi_1}{dy^4} = \frac{\varepsilon\sigma_1}{Pr_\tau}\frac{d^2\psi_0}{dy^2} - i\tilde{k}\varepsilon(Ra_{\tau_0}N_0 + Ra_{\tau_{-1}}N_1),$$

$$\frac{d^2\bar{C}_1}{dy^2} = N_1,$$

$$\frac{d^2N_1}{dy^2} = (2 + \varepsilon\sigma_1)N_0 + y\frac{dN_0}{dy}, \tag{28}$$

with the boundary conditions

$$\frac{d^3\psi_1(1)}{dy^3} - \frac{\varepsilon\sigma_1}{Pr_\tau}\frac{d\psi_0(1)}{dy} = 0, \quad \frac{d^2\psi_1(1)}{dy^2} = 0,$$

$$\frac{dN_1(1)}{dy} - \frac{d\bar{C}_0(1)}{dy} - N_0(1) = 0,$$

$$\bar{C}_1(1) = 0, \quad \frac{d\psi_1(0)}{dy} = 0, \quad \psi_1(0) = 0,$$

$$\frac{dN_1(0)}{dy} = 0, \quad \frac{d\bar{C}_1(0)}{dy} = 0. \tag{29}$$

Then, we will solve the above system of equations with the corresponding boundary condition to get the solution of ψ_1, $\bar{C}_1$, and N_1 at the first-order. The solutions are given in Appendix A.

Similarly, we will solve the system of equations at the second-order using the zeroth and first order solutions which are mentioned in Appendix A.

The first-order solution is the functions of N_1, $\bar{C}_1$, and ψ_1 and we can obtain $\sigma_1 = 0$; i.e., the instability is stationary.

At the second-order solution, we have found σ_2 as follows:

$$\sigma_2 = \varepsilon\tilde{k}^2\left(\frac{13}{360}Ra_{\tau_{-1}} - 1\right). \tag{30}$$

It can be noticed from (30) that the system is unstable to small wavenumber disturbances if $Ra_{\tau_{-1}} > (360/13)$. The resultant instability indicates that it is non-oscillatory. It would be interesting to study the marginal stability in which $\sigma_r = 0$ and we will calculate σ_i. Marginal stability ($\sigma = 0$) occurs when

$$Ra_\tau(\tilde{k}) = \frac{360}{13(SH/Le_\tau)} + O(1). \tag{31}$$

The correction of Ra_{τ_0} to the value of $Ra_\tau(\tilde{k})$ in (31) for marginal stability can now be found in terms of $Ra_{\tau_{-1}}$ and $\tilde{k}^2$ using (30).

C. Linear stability results and discussions

We have studied three sets of parameters, Set 1: $S = 1$, $H = 1$, $Le_\tau = 0.5$, $Pr_\tau = 500$; Set 2: $S = 5$, $H = 4$, $Le_\tau = 1$, $Pr_\tau = 7700$; and Set 3: $S = 10$, $H = 20$, $Le_\tau = 5$, $Pr_\tau = 500$. The dimensionless parameters introduced in this paper are renamed for better readability and are different from the definition of parameters presented in the work of Hillesdon and Pedley[3] (see Nomenclature). The differences are $S \sim \gamma_{HP}$, $\frac{H}{Le_\tau} \sim \beta_{HP}$, $Le_\tau \sim \delta_{HP}$, $Pr_\tau \sim Sc_{HP}$, and $Ra_\tau \sim \Gamma_{HP}$, where HP refers to Hillesdon and Pedley.[3] Figure 2 shows the analytically computed steady-state solutions for oxygen $c(y)$ and cell $n(y)$ concentration density profiles at the variations of S, H, and Le_τ. In the steady-state, diffusion of cells (random cell swimming) balances chemotaxis, while oxygen diffusion is balanced by the consumption of oxygen. The steady-state cell (n) and oxygen (c) distributions depend only on y. Here, two distinct cases can appear. In a shallow chamber, provided that the cutoff $r(c) = 1$, the cells are actively swimming upwards and consuming oxygen. The system is unstable near the free-surface for a certain range of parameters. In the deep chamber case, the oxygen concentration starts to decrease below a certain depth. Under the circumstances, oxygen concentration c becomes smaller than c^*, according to the definition given in Eq. (2). At this moment, for $r(c) = 0$ cells in this oxygen-depleted region (near the bottom) become inactive to swim or to consume oxygen. We have affixed the present study for a shallow chamber only. Here, the results of Hillesdon and Pedley[3] and Chertock *et al.*[4] are considered to compare with our steady-state results presented in Fig. 2. The expressions of the cell concentration in Eq. (18) and the oxygen concentration in Eq. (19) at steady-state in the present study are similar to those of the work of Chertock *et al.*,[4] whereas the steady-state solution of oxygen is different from that of the work of Hillesdon and Pedley.[3] It can be seen that the present steady-state results have good agreement with those of the work of Chertock *et al.*[4] as the authors also studied the two-dimensional chemotaxis system. They numerically investigated the formation of plume patterns and their evolved shapes falling from the flat free-surface, whereas we have performed our investigation for the deformed free-surface. Hillesdon and Pedley[3] studied the 3D chemotaxis system for both deep and shallow chambers with flat free-surface. There is a small difference in the definitions of the parameters between the present study and the study of Hillesdon and Pedley[3] which has been previously mentioned in this section. The discrepancy in curves appeared in Fig. 2(a) due to this reason although the steady-state result for n in Fig. 2(b) shows good agreement. The comparison of steady-state results shown in Figs. 2(c) and 2(d) and Figs. 2(a) and 2(b) are for the three sets of parameters, Set 1: $S = 1$, $H = 1$, $Le_\tau = 0.5$, $Pr_\tau = 500$; Set 2: $S = 5$, $H = 4$, $Le_\tau = 1$, $Pr_\tau = 7700$; and Set 3: $S = 10$, $H = 20$, $Le_\tau = 5$, $Pr_\tau = 500$, respectively. It is clear from the steady-state cell of Fig. 2(d) that the number of cells increases in the direction moving toward the free-surface of the chamber and the oxygen density, shown in Fig. 2(c), is decreased, at the varying parametric values of S and H. The increased value of H leads to instability. The steady-state distributions of cell and oxygen concentrations depend on Le_τ [see Figs. 2(e) and 2(f)], and this shows that as Le_τ increases, the basic flow becomes stabilized because an increased value of D_O corresponds to a more uniform oxygen distribution throughout the system and a smaller gradient of the oxygen concentration causes the micro-organisms
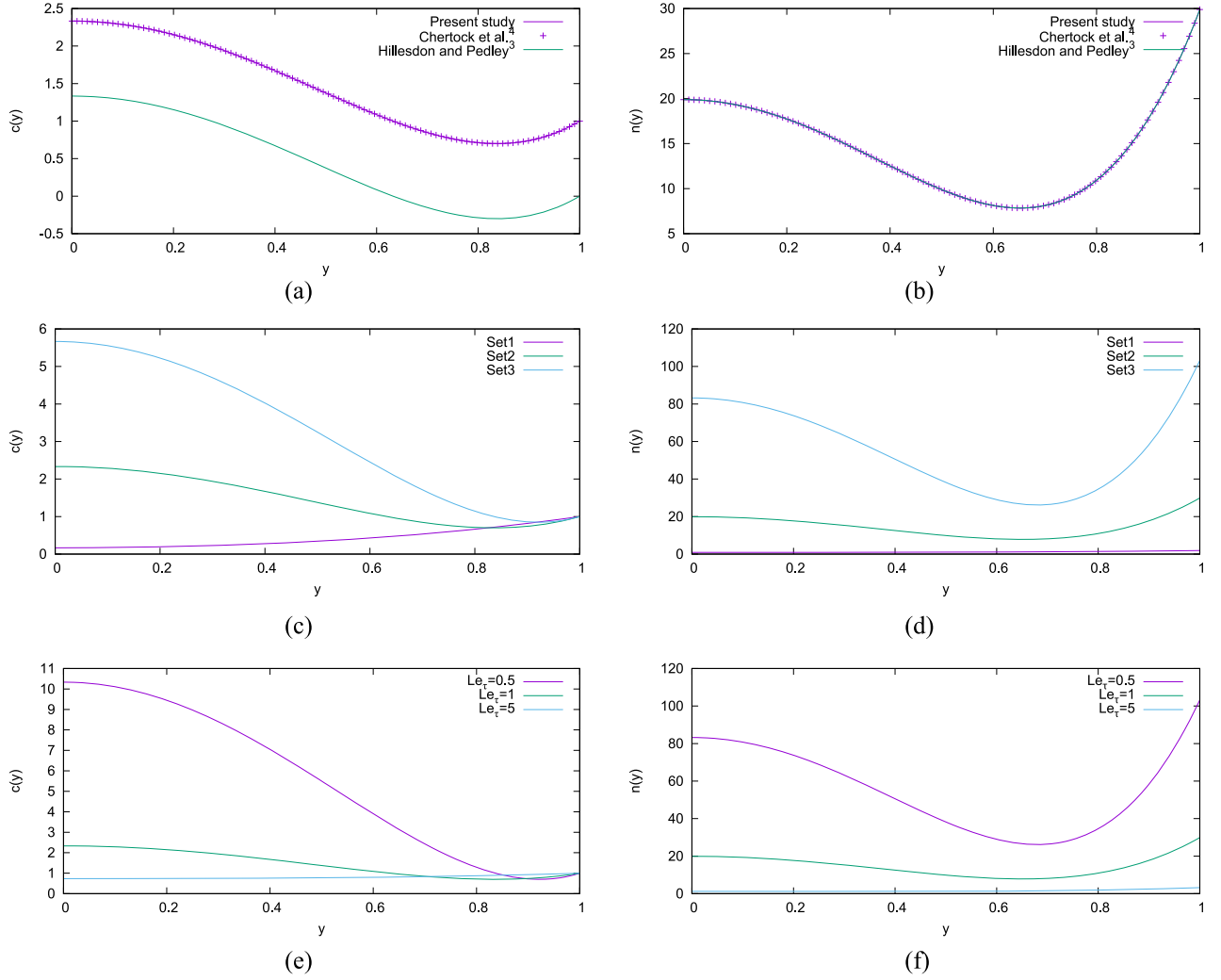
FIG. 2. Dimensionless steady-state (a) oxygen and (b) cell concentration profiles of the present study with the parameters of Set 2. (c) and (d) show the variation of three sets of parameters (Set 1: $S = 1$, $H = 1$, $Le_\tau = 0.5$, $Pr_\tau = 500$; Set 2: $S = 5$, $H = 4$, $Le_\tau = 1$, $Pr_\tau = 7700$; and Set 3: $S = 10$, $H = 20$, $Le_\tau = 5$, $Pr_\tau = 500$). In (e) and (f), Le_τ is varied at parameter Set 2.

to move in the system less rigorously. The values of S and H are fixed to 5 and 4, respectively, for Figs. 2(e) and 2(f). The set of parameters is tested and the analytical results are well compared with the results of Hillesdon and Pedley[3] where the linear stability analysis of (21a)–(21c) predicts the loss of stability and the onset of the convection pattern with a critical wavenumber $k_c \approx 1.368$, i.e., with wavelength $\lambda_c = 2\pi/k_c \approx 4.593$ for the parameter Set 2.

The linear stability of the steady-state depends on the value of the Rayleigh number Ra_τ. If Ra_τ is less than a critical value of Ra_{τ_c}, the steady-state is stable, whereas if the value of Ra_τ is greater than Ra_{τ_c}, the steady-state is unstable. Ra_{τ_c} depends on the wavenumber k of the shallow water wave disturbance. Ra_{τ_c} has its minimum value at the most unstable wavenumber k_c. A further increment of Ra_τ leads to the first bifurcation. Hillesdon and Pedley[3] calculated the critical values of k and Γ, which depend on δ and $\beta\gamma$, whereas in the present study, the critical values of k and Ra_τ depend on S and H/Le_τ. k_c also depends on ε. Some critical values of Ra_{τ_c} and k_c, which vary with SH/Le_τ, are presented in Table I. From the first row of data in Table I, the values Ra_{τ_c} and k_c are seen

to be 524.738 and 3.85 for $Le_\tau = 1$, $SH = 0.05$, whereas in the work of Hillesdon and Pedley,[3] the values of Ra_{τ_c} and k_c are calculated as 1.025×10^4 and 1.37 for $\delta_{HP} = 1$, $\beta_{HP}\gamma_{HP} = 0.05$. It is concluded that our system subject to the deformed free-surface reaches the criticality before Hillesdon and Pedley's[3] system under the assumption of flat free-surface.

TABLE I. Values of Ra_{τ_c}, k_c evaluated for the shallow chamber case. Here, -HP represents the values from Hillesdon and Pedley[3] and -Present represents the values of the present study.

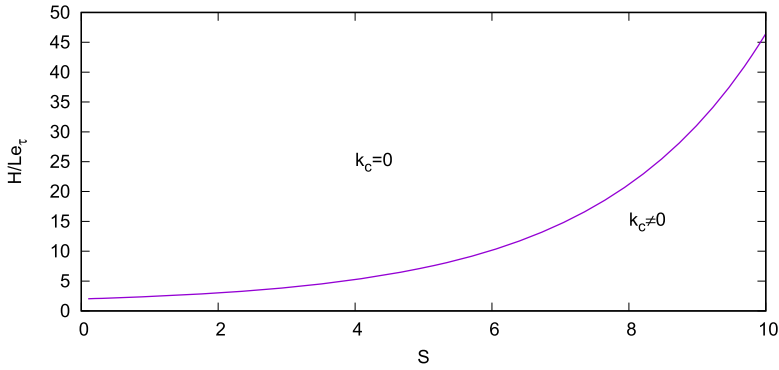| Le_τ	SH	Ra_{τ_c}-HP	k_c-HP	Ra_{τ_c}-Present	k_c-Present	ε
1	0.05	1.02×10^4	1.37	524.738	3.853 95	0.1
1	0.05			524.738	1.926 97	0.2
1	0.05			524.738	0.770 79	0.5
1	1	625	1.58	12.613	0.721 76	0.1
1	10	200	1.90	120.596	0.072 54	0.1
1	50	328	1.94	709.072	0.014 51	0.1
1	100	522	1.91	1447.160	0.007 25	0.1
5	10	221	1.24	13.535	0.362 68	0.1
5	50	354	1.35	120.596	0.007 25	0.1

FIG. 3. Parameter regions where the critical wavenumber k_c is zero or non-zero.

Especially the values of critical wavenumber k_c have either zero or non-zero value depending on the range of parameters considered (shown in Fig. 3).

Some interesting results of $\bar{C}$ and N profiles at $k_c \neq 0$ and $k_c = 0$ have been shown in Figs. 4(a) and 4(b), respectively. Figures 4(c) and 4(e) and Figs. 4(d) and 4(f) show $\bar{C}$ and N distributions, respectively, for the computed values of Ra_{τ_c} and k_c. It has been clear from Fig. 4, for the parametric values of

$Le_\tau = 1$, $S = 5$, $H = 4$, and $Pr_\tau = 7700$, that the chemotaxis system is always stable for $k_c = 0$. However, for $k_c \neq 0$, it stabilizes close to the free-surface. The small deviation between the computed values of Ra_{τ_c} and a significant deviation for k_c occur when the value of H increases. A possible source of differences originates from the fact that the shallow chamber equations are not uniformly valid as the transition is reached. Since in the transition region the steady-state value of $\bar{C}$ is zero
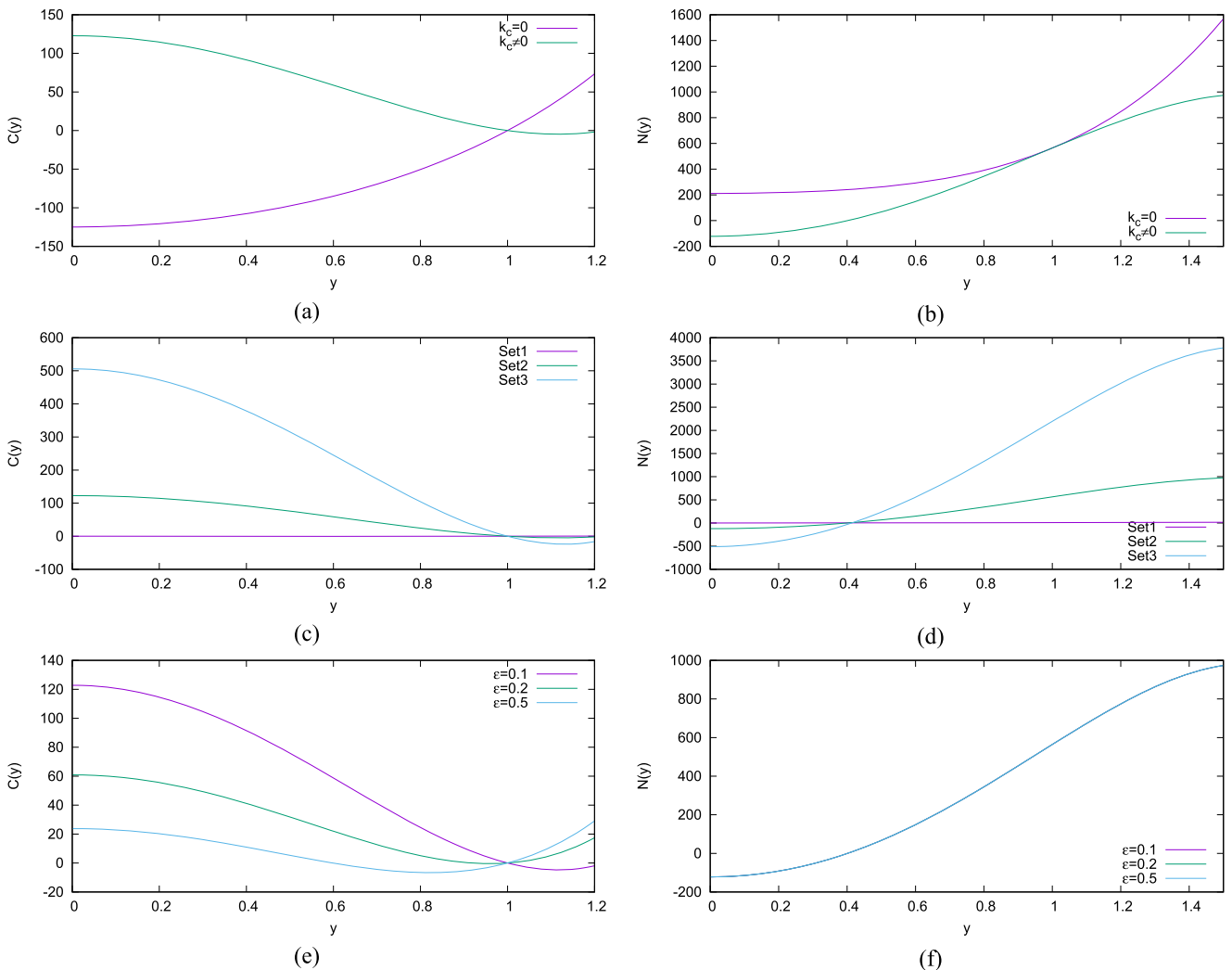

FIG. 4. Different characteristics of $N_i(y)$ and $\bar{C}_i(y)$ perturbation profiles correspond to the values of Ra_{τ_c} and k_c, for the shallow chamber (a) and (b) at Set 2; (c) and (d) for different sets of parameters (Set 1: $S = 1$, $H = 1$, $Le_\tau = 0.5$, $Pr_\tau = 500$; Set 2: $S = 5$, $H = 4$, $Le_\tau = 1$, $Pr_\tau = 7700$; and Set 3: $S = 10$, $H = 20$, $Le_\tau = 5$, $Pr_\tau = 500$) and (e) and (f) with the variation of ε at Set 2.

so that the perturbation must be taken smaller to prevent the occurrence of negative values of $\bar{C}$. To illustrate this argument, we have compared the real parts of the N, $\bar{C}$ and the imaginary part of ψ solutions (as the real part of ψ solution is always stable) and another example of the transition curve ($Le_\tau = 1$, $S = 5$, $H/Le_\tau = 4$) with the N, $\bar{C}$. We have varied the length of the shallow chamber in our study by controlling the parameter ε. Figures 4(e) and 4(f) show the stabilizing nature as the length of the chamber increases.

The comparison for $k_c = 0$ and $k_c \neq 0$ has been shown in Fig. 5. Both the curves show the stability near the interface, but unstable chemotaxis motion can be observed in the main body of the chamber. Apart from the discontinuous jump in the N distribution obtained at $S = 5$, $H = 4$, and $Le_\tau = 1$, the most striking difference is encountered, as expected, in the $\bar{C}$ distributions. At $y = 0$, the zero-cell-flux condition is satisfied for the case with $S = 5$. Therefore, a noticeable difference can be observed between the profiles of N, $\bar{C}$, and ψ and, consequently, the values of Ra_{τ_c} and k_c. In Fig. 5(d), ψ profiles have been shown with the variation of ε.

The results shown in Fig. 6 are the computed values of Ra_{τ_c} with the corresponding values of k_c which vary with $\frac{SH}{Le_\tau}$. Two interesting features are re-exhibited. In Fig. 6(a), we can see that the neutral curves for different values of Le_τ diverge as the wavenumber increases, in spite of the fact that the steady-state is homogeneous. The value of Ra_τ, for a given k, is larger for $Le_\tau = 5$ than for $Le_\tau = 1$; i.e., an increase in Le_τ apparently stabilizes the system. Second, a more important comparison is made between the cases with different values of SH for steady-state cell and oxygen distributions and the value of $Le_\tau = 1$ (can be seen in Fig. 2). Moreover, from Table I, it can be seen that for

large values of $\frac{SH}{Le_\tau}$, the system should be more unstable. $Ra_{\tau c}$ first falls as $\frac{SH}{Le_\tau}$ is increased and then rises again. Also, k_c has a maximum value, and $Ra_{\tau c}$ has the minimum value, although not at the same value of $\frac{SH}{Le_\tau}$. The above mentioned behavior is furthermore examined by plotting the values of $Ra_{\tau c}$ and k_c against $\frac{SH}{Le_\tau}$ for different values of Le_τ in Figs. 6(a) and 6(b) and for different values of ε in Fig. 6(c). For each value of Le_τ and ε, the overall minimum values of $Ra_{\tau c}$ and k_c occur when $\frac{SH}{Le_\tau} \approx 0.9636$.

Figure 7(a) shows the curve of $Ra_\tau(k)$ for the shallow chamber corresponding to $S = 1$, $H/Le_\tau = 1$; $S = 1$, $H/Le_\tau = 4$; and $S = 5$, $H/Le_\tau = 7$. The curves are tantamount, except for the wavenumbers smaller than 1, where Ra_τ has significantly different values, because it may be possible that for this range of values the corresponding dimensional wavelength, λ, is relatively large in comparison of the shallow chamber height h. Therefore the disturbances will infiltrate to the bottom of the shallow chamber and will affect the stability of the region. The curves of $Ra_\tau(k)$ are shown for the case $H/Le_\tau \geqslant 7$ in Fig. 7(a). The qualitative behavior is tantamount in each case; as k increases from zero, the Rayleigh number Ra_τ increases swiftly upwards from its minimum value and as H/Le_τ increases so does the value of Ra_{τ_c}. The dependence of σ_i on k for the values of $Le_\tau = 0.5$, 1, and 5 is tested and shown in Fig. 7(b) for $H = 1$, $S = 1$, and $\varepsilon = 0.1$. The frequency of oscillation corresponding to a wavenumber is increasing as Le_τ decreases. It can be seen in Fig. 7(b) that the peak of temporal growth is increased as Le_τ is decreased, indicating the stabilizing effect. In Figs. 7(c) and 7(d), ε is varied indicating that the wavenumber increases with the length of the chamber as well as the peak of temporal growth.
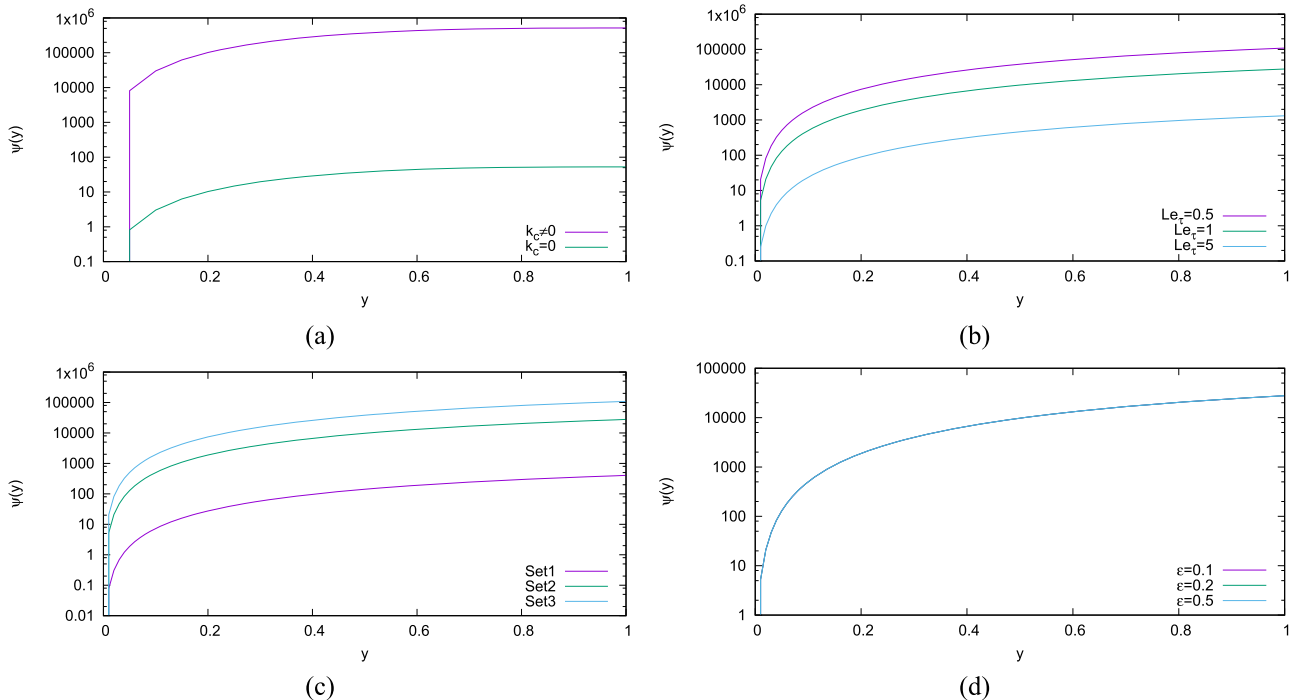

FIG. 5. Different characteristics of $\psi(y)$ perturbation profiles correspond to the values of Ra_{τ_c} and k_c for the shallow chamber: (a) with $k_c = 0$ and $k_c \neq 0$ at parameter Set 2; (b) with the variation of Le_τ at parameter Set 2; (c) with the variation of sets of parameters (Set 1: $S = 1$, $H = 1$, $Le_\tau = 0.5$, $Pr_\tau = 500$; Set 2: $S = 5$, $H = 4$, $Le_\tau = 1$, $Pr_\tau = 7700$; and Set 3: $S = 10$, $H = 20$, $Le_\tau = 5$, $Pr_\tau = 500$); and (d) with the variation of ε at Set 2.
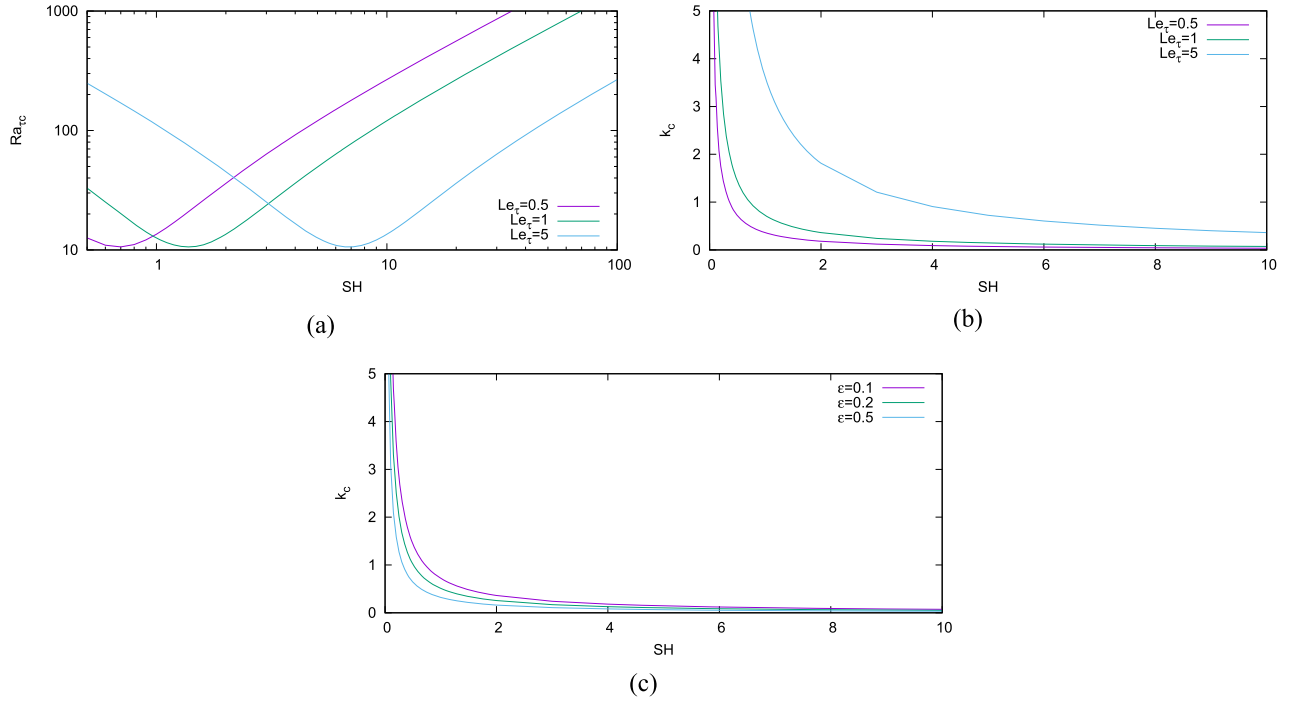
FIG. 6. (a) $Ra_{\tau c}$ is computed for the varying values of Le_τ; (b) the corresponding values of k_c for varying Le_τ; and (c) the variation of ε at $Le_\tau = 1$. The minimum value of the curve is $\frac{SH}{Le_\tau} \approx 1.036$.
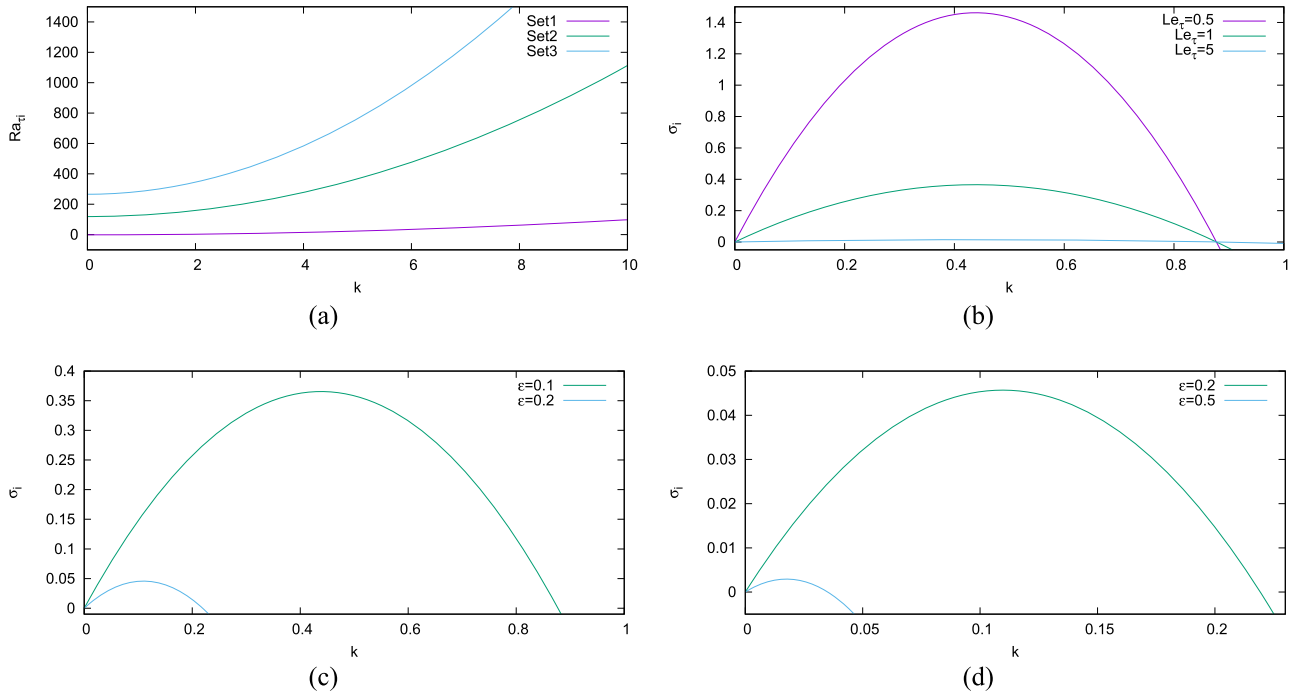

FIG. 7. $Ra_{\tau_i}(k)$ and $\sigma_i(k)$ curves for the shallow chamber at (a) the varying sets of parameters (Set 1: $S = 1$, $H = 1$, $Le_\tau = 0.5$, $Pr_\tau = 500$; Set 2: $S = 5$, $H = 4$, $Le_\tau = 1$, $Pr_\tau = 7700$; and Set 3: $S = 10$, $H = 20$, $Le_\tau = 5$, $Pr_\tau = 500$); (b) Le_τ varied and $S = 5$, $H = 4$, $\varepsilon = 0.1$ are fixed; and [(c) and (d)] ε varied and $S = 5$, $H = 4$, $Le_\tau = 1$ are fixed.

IV. WEAKLY NONLINEAR STABILITY ANALYSIS

The linear stability theory is an initial step in the understanding of the pattern formation. However, it provides only a rough idea about the pattern formation. From linear stability analysis, we can determine the conditions of the infinitesimal

disturbances at the onset of instability by the parameters on the system and can choose the length scale of the pattern formation. Additionally, a significant physical role of pattern formation due to cross-diffusion can be explained. The nonlinear stability analysis would help us to predict the amplitude and the types of pattern formation in the system. Therefore,

we must perform a weakly nonlinear stability analysis based on the method of multiple scales.

The objective of the weakly nonlinear stability analysis is to predict the patterns formed near the critical Rayleigh number. From the linear stability analysis, we can only determine the initial behavior of ψ, N, and C about the uniform steady-state when the steady-state is driven unstable to spatially small perturbations. At the onset of instability, the disturbances will be expressed and characterized by a particular wavenumber. However, the pattern formation through convection cells is entirely unspecified.

In bioconvection, a density stratification appears because of the difference in the densities of the bacteria and fluid which surpass the threshold value controlled by the viscosity and the diffusivity of the cell/oxygen. Then the various forms of a regular pattern will appear in convection sets. Many theoretical, experimental, and numerical investigations were devoted to the study of buoyancy-driven instability after the pioneering studies of Bénard in 1900 and Rayleigh in 1916. Some studies are concerned about the development of different pattern formation above the linear convective threshold. It would be noteworthy to mention that under Boussinesq approximation with the linear variation of the density, rolls are found stable above the threshold onset. However, hexagons are preferred over rolls when the Boussinesq approximation is invalid.

In this problem, we will carry out a nonlinear asymptotic analysis by expanding the 2D system into 3D (consider z as the horizontal coordinate) and obtain the solutions to $O(\varepsilon)$ (and to higher orders) which are valid for all time. The framework of the analytical procedure will be prepared, using a multi-scale asymptotic analysis for determining the small perturbation solutions valid for all time of the three-dimensional system. We have expanded the variables in terms of a small parameter ε. At each order in ε, a solvability condition is derived which gives rise to an equation suitable for depicting the evolution of the pattern amplitude. A series expansion with respect to ε and truncation of the series after a finite number of terms is the basic idea of the so-called weakly nonlinear theory.

Stability analysis on the dynamical system of NS-KS equations starts with perturbing $\mathbf{u}(=u, v, w)$ and p in terms of small parameter ε in the form

$$\mathbf{u} = \mathbf{u}_0 + \varepsilon \mathbf{u}_1 + \varepsilon^2 \mathbf{u}_2 + \cdots, \tag{32a}$$

$$p = p_0 + \varepsilon p_1 + \varepsilon^2 p_2 + \cdots. \tag{32b}$$

By substituting the perturbed velocity field into the dimensionless governing equation of the 3D system for n and c, by virtue of the order analysis we are led to know that c and n take the following perturbation forms provided that convection and diffusion take the same order of $O(\varepsilon)$:

$$n = n_0 + \varepsilon n_1 + \varepsilon^2 n_2 + \cdots, \tag{33a}$$

$$c = c_0 + \varepsilon c_1 + \varepsilon^2 c_2 + \cdots. \tag{33b}$$

Stability analysis is followed by substituting Eqs. (32) and (33) into the y-momentum equation of the 3D system (after eliminating u, v, and p), subject to the Boussinesq assumption, to yield the resultant equation written in terms of ε, ε^2, and

so on. The nonlinear control parameter Ra_τ can be perturbed as

$$Ra_\tau = Ra_{\tau c} + \varepsilon Ra_{\tau 1} + \cdots. \tag{34}$$

It is noted that the above equation holds true provided that the terms (v, n, c) have the same order of ε.

We study the evolution of the system over a slow time scale T, where $T = \varepsilon t$. Then, substitute the expanded variables (32)–(34) into Eq. (6). We obtain the steady-state equations for $n(y)$ and $c(y)$ at $O(1)$. At $O(\varepsilon)$, we obtain the system of linear equations where the variables n_1, c_1, and v_1 are expressed as

$$v_1 = V(y)\Re\left(A_1(T)e^{ikz} + A_2(T)e^{ik(-\frac{\sqrt{3}}{2}x - \frac{1}{2}z)}\right.$$
$$\left. + A_3(T)e^{ik(\frac{\sqrt{3}}{2}x - \frac{1}{2}z)}\right), \tag{35a}$$

$$n_1 = N(y)\Re\left(A_1(T)e^{ikz} + A_2(T)e^{ik(-\frac{\sqrt{3}}{2}x - \frac{1}{2}z)}\right.$$
$$\left. + A_3(T)e^{ik(\frac{\sqrt{3}}{2}x - \frac{1}{2}z)}\right), \tag{35b}$$

$$c_1 = C(y)\Re\left(A_1(T)e^{ikz} + A_2(T)e^{ik(-\frac{\sqrt{3}}{2}x - \frac{1}{2}z)}\right.$$
$$\left. + A_3(T)e^{ik(\frac{\sqrt{3}}{2}x - \frac{1}{2}z)}\right). \tag{35c}$$

The amplitudes $A_i(i = 1, 2, 3)$ for rolls become $A_1 = A$, $A_2 = A_3 = 0$ and for hexagons $A_1 = A_2 = A_3 = A$.

At $O(\varepsilon^2)$, the problem gives rise to a solvability condition as follows:

$$\int \theta \cdot RHS dx + \int\int \left(\theta_2 n_1 \frac{\partial c_1}{\partial y}\right)\bigg|_{y=0} dx dz = 0, \tag{36}$$

where the first-order adjoint $\theta = (\theta_1, \theta_2, \theta_3)$ denotes the variables (v_1, n_1, c_1) and RHS is the right-hand side of the $O(\varepsilon^2)$ equations, which consist of known first-order functions. In Eq. (36), three solvability conditions can be obtained by setting $\theta = \Theta \bar{A}_1 e^{-ikz}$, $\theta = \Theta(y)\bar{A}_2 e^{ik(\frac{\sqrt{3}}{2}x + \frac{1}{2}z)}$, and $\theta = \Theta \bar{A}_3 e^{ik(-\frac{\sqrt{3}}{2}x + \frac{1}{2}z)}$, where $\Theta(y) = (\Theta_1, \Theta_2, \Theta_3)$ and an overbar "‾" represents the complex conjugate. After substituting these into the known first-order functions and integrating from 0 to $4\pi/\sqrt{3}k$ with respect to x and from 0 to $4\pi/k$ with respect to z, one can derive

$$\xi_1 \frac{dA_1}{dT} + Ra_{\tau 1}\xi_3 + \xi_2 \bar{A}_2 \bar{A}_3 = 0. \tag{37a}$$

Two more equations are also obtained for A_2 and A_3 as follows:

$$\xi_1 \frac{dA_2}{dT} + Ra_{\tau 1}\xi_3 + \xi_2 \bar{A}_1 \bar{A}_3 = 0, \tag{37b}$$

$$\xi_1 \frac{dA_3}{dT} + Ra_{\tau 1}\xi_3 + \xi_2 \bar{A}_1 \bar{A}_2 = 0. \tag{37c}$$

The ξ_i denote the integrals of the known first-order functions which are presented in Appendix B.

For steady rolls where $A_1 = A$, $A_2 = A_3 = 0$, and $dA/dT = 0$, the existing solvability conditions imply that $Ra_{\tau 1} = 0$. This indicates that for rolls we should have defined ε by $Ra_\tau - Ra_{\tau c} = \varepsilon^2 Ra_{\tau 2}$ and rescaled time by $T = \varepsilon^2 t$.

For steady hexagons where $A_1 = A_2 = A_3 = A$ and $dA/dT = 0$, we have

$$Ra_{\tau 1} = -\frac{\xi_2}{\xi_3}A. \tag{38}$$

A stability analysis of (37a) exhibits that both the branches are unstable of this bifurcation. But at a higher order, one among these branches may become stable. So, we rescale Ra_τ and t to capture this behavior which includes the third-order

cubic terms as well as the second-order quadratic terms in the amplitude equations. Then, from Eq. (38), $Ra_\tau - Ra_{\tau c}$ is of $O(\varepsilon^2)$.

We redefine $Ra_\tau = Ra_{\tau c} + \varepsilon^2 Ra_{\tau 2}$ and consider $T = \varepsilon^2 t$. In this process, we obtain the steady-state equation again at $O(1)$ and the linear equations at $O(\varepsilon)$. Then we include both the $O(\varepsilon^2)$ and $O(\varepsilon^3)$ terms in the amplitude equations. Therefore having both the terms $O(\varepsilon^2)$ and $O(\varepsilon^3)$ together, we can derive the following solvability condition:

$$
\varepsilon^3 \int \theta \cdot \overline{RHS} \mathrm{d}x + \varepsilon^2 \int \theta \cdot \widetilde{RHS} \mathrm{d}x
$$
$$
= -\varepsilon^3 \int \int \left(\theta_2 n_1 \frac{\partial c_2}{\partial y} + \theta_2 n_2 \frac{\partial c_1}{\partial y} \right)\Big|_{y=0} \mathrm{d}x\mathrm{d}z
$$
$$
- \varepsilon^2 \int \int \left(\theta_2 n_1 \frac{\partial c_1}{\partial y} \right)\Big|_{y=0} \mathrm{d}x\mathrm{d}z, \tag{39}
$$

where the terms $\overline{RHS}$ and $\widetilde{RHS}$ contain the known first- and second-order functions. Then, we substitute these functions into Eq. (39) to obtain the three amplitude equations. The first one is

$$
\varepsilon^3 \xi_1 \frac{\mathrm{d}A_1}{\mathrm{d}T} + \varepsilon^3 Ra_{\tau 2} \xi_3 A_1 + \varepsilon^3 \xi_6 A^2{}_1 \bar{A}_1
$$
$$
+ \varepsilon^3 \xi_5 A_1 (A_2 \bar{A}_2 + A_3 \bar{A}_3) + \varepsilon^2 \xi_2 \bar{A}_2 \bar{A}_3 = 0, \tag{40a}
$$

and two more equations obtained for A_2 and A_3 are

$$
\varepsilon^3 \xi_1 \frac{\mathrm{d}A_2}{\mathrm{d}T} + \varepsilon^3 Ra_{\tau 2} \xi_3 A_2 + \varepsilon^3 \xi_6 A^2{}_2 \bar{A}_2
$$
$$
+ \varepsilon^3 \xi_5 A_2 (A_1 \bar{A}_1 + A_3 \bar{A}_3) + \varepsilon^2 \xi_2 \bar{A}_1 \bar{A}_3 = 0, \tag{40b}
$$
$$
\varepsilon^3 \xi_1 \frac{\mathrm{d}A_3}{\mathrm{d}T} + \varepsilon^3 Ra_{\tau 2} \xi_3 A_3 + \varepsilon^3 \xi_6 A^2{}_3 \bar{A}_3
$$
$$
+ \varepsilon^3 \xi_5 A_3 (A_1 \bar{A}_1 + A_2 \bar{A}_2) + \varepsilon^2 \xi_2 \bar{A}_1 \bar{A}_2 = 0. \tag{40c}
$$

In the above equations, ξ_1, ξ_2, and ξ_3 are the same as before and all ξ_i's ($i = 1, 2, 3$) including ξ_5 and ξ_6 are given in Appendix B. If we assume that $\xi_1 \neq 0$, then we can write $\tilde{\xi}_2 = \frac{\xi_2}{\xi_1}$, $\tilde{\xi}_3 = \frac{\xi_3}{\xi_1}$ and the amplitude equation becomes

$$
\frac{\mathrm{d}A_1}{\mathrm{d}T} + Ra_{\tau 2} \tilde{\xi}_3 A_1 + \tilde{\xi}_6 A^2{}_1 \bar{A}_1
$$
$$
+ \tilde{\xi}_5 A_1 (A_2 \bar{A}_2 + A_3 \bar{A}_3) + \frac{\tilde{\xi}_2}{\varepsilon} \bar{A}_2 \bar{A}_3 = 0. \tag{41a}
$$

Two additional equations obtained for A_2 and A_3 are as follows:

$$
\frac{\mathrm{d}A_2}{\mathrm{d}T} + Ra_{\tau 2} \tilde{\xi}_3 A_2 + \tilde{\xi}_6 A^2{}_2 \bar{A}_2
$$
$$
+ \tilde{\xi}_5 A_2 (A_1 \bar{A}_1 + A_3 \bar{A}_3) + \frac{\tilde{\xi}_2}{\varepsilon} \bar{A}_1 \bar{A}_3 = 0, \tag{41b}
$$
$$
\frac{\mathrm{d}A_3}{\mathrm{d}T} + Ra_{\tau 2} \tilde{\xi}_3 A_3 + \tilde{\xi}_6 A^2{}_3 \bar{A}_3
$$
$$
+ \tilde{\xi}_5 A_3 (A_1 \bar{A}_1 + A_2 \bar{A}_2) + \frac{\tilde{\xi}_2}{\varepsilon} \bar{A}_1 \bar{A}_2 = 0. \tag{41c}
$$

For regular time-independent hexagons with $A_1 = A_2 = A_3 = A$, the above amplitude equation gives

$$
\varepsilon^2 Ra_{\tau 2} = -\frac{(2\tilde{\xi}_5 + \tilde{\xi}_6)}{\tilde{\xi}_3} \varepsilon^2 A^2 - \frac{\tilde{\xi}_2}{\tilde{\xi}_3} \varepsilon A. \tag{42}
$$

Then, Ra_τ will be obtained as

$$
Ra_\tau = Ra_{\tau c} - \varepsilon \left(\frac{\tilde{\xi}_2}{\tilde{\xi}_3} \right) A - \varepsilon^2 \frac{(2\tilde{\xi}_5 + \tilde{\xi}_6)}{\tilde{\xi}_3} A^2. \tag{43}
$$

Equation (43) justifies the mixing of the second- and third-order terms only if the ratio $\xi_2/(2\xi_5 + \xi_6)$ is of $O(\varepsilon)$. A stability analysis of (41a) shows that the conditions for hexagons to be stable only when

$$
\tilde{\xi}_2 A < 0, \quad -\frac{\tilde{\xi}_2}{\varepsilon} A - 2\tilde{\xi}_6 A^2 - 4\tilde{\xi}_5 A^2 < 0,
$$
$$
2\frac{\tilde{\xi}_2}{\varepsilon} A - 2\tilde{\xi}_6 A^2 + 2\tilde{\xi}_5 A^2 < 0. \tag{44}
$$

For steady rolls ($A_1 = A$, $A_2 = A_3 = 0$), the solvability condition holds provided that

$$
Ra_{\tau 2} = -\frac{\tilde{\xi}_6}{\tilde{\xi}_3} A^2. \tag{45}
$$

This is a pitchfork bifurcation which has the conditions for the stable branches only if

$$
\tilde{\xi}_6 > 0, \quad \frac{\tilde{\xi}_2}{\varepsilon} A + (\tilde{\xi}_6 - \tilde{\xi}_5) A^2 < 0, \quad -\frac{\tilde{\xi}_2}{\varepsilon} A + (\tilde{\xi}_6 - \tilde{\xi}_5) A^2 < 0. \tag{46}
$$

The mixed mode solution branches are obtained of the form $A_1 = A$, $A_2 = A_3 = B$ and can link the roll and hexagon branches. These mixed mode solution branches will turn to rolls when $B = 0$ and regular hexagon when $B = A$. The stability analysis revealed that these mixed mode solution branches are always unstable.

V. BIFURCATION THEORY

In this section, we have thoroughly studied the bifurcation diagram depending on the values of $\tilde{\xi}_2$, $\tilde{\xi}_3$, $\tilde{\xi}_5$, and $\tilde{\xi}_6$. The shape, the amplitude, and the stability properties of the bifurcation diagrams are drawn in Fig. 8 and discussed here. It can be seen from the figures that there are changes in the amplitude of the disturbances, A, as the Rayleigh number Ra_τ is increased. For the sake of simplicity, the roll and hexagon branches are drawn as both of them fit in the same lattice. Moreover, in reality, both the branches are placed in the different planes and do not intersect each other, whereas the mixed mode branches intersect the other branches at the points are marked as dots in the figures. The hexagon branches with positive and negative A represent the up- and down-hexagon, respectively. But there is no difference between the rolls with positive or negative A.

A. Pitchfork bifurcation

All the possible roll, hexagon, and mixed mode branches are drawn in Fig. 8. It has been observed that if $\tilde{\xi}_2 < 0$, $\tilde{\xi}_3 < 0$, $\tilde{\xi}_6 > \tilde{\xi}_5 > 0$, the bifurcation diagram will correspond to Fig. 8(a). It can be easily seen in the figure that the hexagon branch is stable with positive A. Therefore, the first anticipated pattern can be an up-hexagon of finite amplitude where the flows move upward in the center and downward at the edges. The hexagon branch bifurcates supercritically. Initially, the hexagon branch is unstable and bifurcates sub-critically to the roll branch. The portion of the unstable hexagon branch with negative A indicates a down-hexagon in which the flows move downward in the center and upward at the edges. The rolls are supercritical and always unstable. A mixed mode branch intersects the unstable hexagon
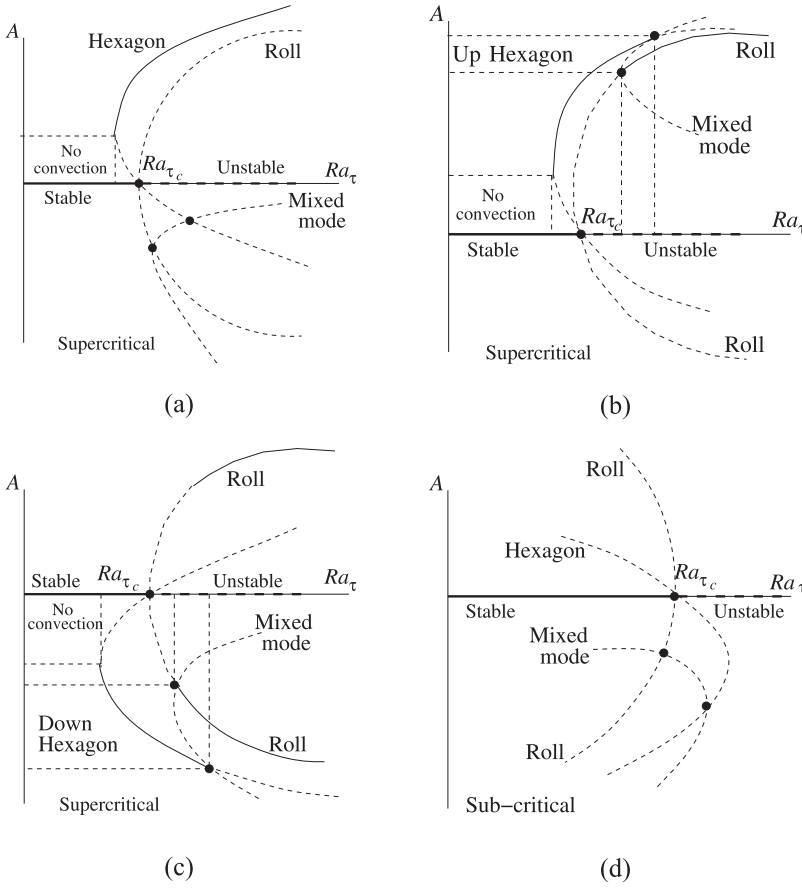
FIG. 8. Bifurcation diagrams. A graphical representation of the amplitude of the nonlinear perturbations A versus the Rayleigh number Ra_τ where solid and dashed lines correspond to the linearly stable and unstable branches, respectively. Bifurcation diagrams [using Eq. (43)] according to third-order nonlinear theory for rolls, hexagons, and mixed mode solutions. "Up" hexagons have $A > 0$ and "down" hexagons have $A < 0$. (a) $\tilde{\xi}_2 < 0$, $\tilde{\xi}_3 < 0$, $\tilde{\xi}_6 > \tilde{\xi}_5 > 0$; (b) $\tilde{\xi}_2 < 0$, $\tilde{\xi}_3 < 0$, $\tilde{\xi}_5 > \tilde{\xi}_6 > 0$; (c) $\tilde{\xi}_2 > 0$, $\tilde{\xi}_3 < 0$, $\tilde{\xi}_5 > \tilde{\xi}_6 > 0$; and (d) $\tilde{\xi}_2 < 0$, $\tilde{\xi}_3 < 0$, $\tilde{\xi}_5 < \tilde{\xi}_6 < 0$.

and roll branches at the points where their respective stability changes.

If $\tilde{\xi}_2 < 0$, $\tilde{\xi}_3 < 0$, $\tilde{\xi}_5 > \tilde{\xi}_6 > 0$, the bifurcation diagram will correspond to Fig. 8(b). The roll branch bifurcates supercritically. Initially, the hexagon branch is stable, but it loses stability as Ra_τ increases and bifurcates sub-critically to the roll branch. The roll branch becomes stable. The portion of the stable hexagon branch with positive A indicates an up-hexagon in which the flows move upward in the center and downward at the edges. The rolls are supercritical, and a portion of the branch is stable at positive A. Again in this figure, a mixed mode branch intersects the stable hexagon and unstable roll branches at the points where their respective stability changes.

If $\tilde{\xi}_2 > 0$, $\tilde{\xi}_3 < 0$, $\tilde{\xi}_5 > \tilde{\xi}_6 > 0$, the bifurcation diagram will correspond to Fig. 8(c), which is just the inverse of Fig. 8(b). Here the first transition is to the down-hexagons which lose stability to roll at higher values of Ra_τ. The roll and hexagon branches are again intersected at the points where the nature of the stability changes. The portion of the stable hexagon branch with negative A indicates a down-hexagon in which the flows move downward in the center and upward at the edges. In all the above cases, the first noticeable pattern of the hexagon branch would be either upward or downward.

If $\tilde{\xi}_2 < 0$, $\tilde{\xi}_3 < 0$, and $\tilde{\xi}_5 < \tilde{\xi}_6 < 0$, the bifurcation diagram will correspond to Fig. 8(d). In this figure, the mixed mode pattern has been shown to be always unstable intersecting at a point of unstable roll and hexagon branches. Here,

the branches led to a sub-critical pitchfork bifurcation. In this case, both the hexagon and roll branches are unstable. Physically, a possibility of their transition to another steady-state pattern or unsteady pattern may be expected. The nonlinear stability analysis is also carried out for square lattice, and a pitchfork bifurcation is found. The stability of bifurcation branches (either sub- or supercritical) depends on the values of $\tilde{\xi}_i$.

This type of amplitude Eq. (41a) is the most commonly used equation for the bioconvection problem and has been widely studied. The hexagon patterns (either up or down) found in this study depend on the values of ξ_i which must be solved numerically. We have taken the values of the parameters mentioned in Table I to calculate ξ_i numerically. The numerically computed values of ξ_i are presented in Table II. We have taken the values of the critical Rayleigh number Ra_{τ_c} from the linear stability analysis (see Table I) as the initial data for the numerical computation of nonlinear systems. In Table II, $Ra_{\tau_{cP}}$ is the critical pitchfork Rayleigh number.

B. Numerically evaluated results of hexagon pattern

The bifurcation diagram depends on the values of ξ_i ($i = 1, 2, 3, 5, 6$) in Eq. (41a) which are found by solving the $O(\varepsilon)$ and $O(\varepsilon^2)$ equations numerically considering $k_c \neq 0$. Then we evaluated the integrals presented in Appendix B. The values of k_c, Ra_τ, and ξ_i depend on S, H, Le_τ, and Pr_τ.

Basically, the system of $O(\varepsilon)$ equations is an eigenvalue problem with Ra_{τ_c} as the eigenvalue. So, an extra arbitrary

TABLE II. Numerically evaluated results of hexagon patterns in a pitchfork bifurcation.

Le_τ	SH	Pr_τ	Ra_{τ_c}	k_c	ε	$Ra_{\tau_{cP}}$	ξ_1	ξ_2	ξ_3	ξ_5	ξ_6	Bifurcation	Pattern
1	0.05	7700	524.738	3.853 95	0.1	1625.45	0.689	2.889	-1.98×10^{-4}	3575.8	3214.21	Super-critical	Down hexagon
1	0.05	7700	524.738	1.926 97	0.2	1763.40	0.752	3.105	-2.01×10^{-4}	3982.5	3540.57	Super-critical	Down hexagon
1	0.05	7700	524.738	0.770 79	0.5	1531.90	0.978	3.658	-2.56×10^{-4}	4521.7	3925.42	Super-critical	Down hexagon
1	0.05	500	524.738	3.853 95	0.1	1620.70	0.715	2.971	-1.99×10^{-4}	3569.5	3221.51	Super-critical	Down hexagon
1	1	7700	12.613	0.721 76	0.1	27.46	0.471	-0.515	-2.19×10^{-3}	5.925	6.015	Super-critical	Up hexagon
1	1	500	12.613	0.721 76	0.1	27.48	0.475	-0.512	-2.19×10^{-3}	5.813	6.018	Super-critical	Up hexagon
1	10	7700	120.596	0.072 54	0.1	1256.80	0.171	-1.91×10^{-3}	-7.45×10^{-3}	5.19×10^{-2}	9.45×10^{-3}	Super-critical	Up hexagon
1	10	500	120.596	0.072 54	0.1	1260.40	0.174	-1.89×10^{-3}	-7.45×10^{-3}	5.16×10^{-2}	9.43×10^{-3}	Super-critical	Up hexagon
1	50	7700	709.072	0.014 51	0.1	1846.20	0.095	-1.12×10^{-3}	-9.85×10^{-3}	1.01×10^{-2}	1.82×10^{-3}	Sub-critical	Unstable hexagon
1	50	500	709.072	0.014 51	0.1	1890.00	0.098	-1.11×10^{-3}	-9.85×10^{-3}	1.0×10^{-2}	1.85×10^{-3}	Sub-critical	Unstable hexagon
5	10	7700	13.535	0.362 68	0.1	529.82	0.257	-0.314	-1.18×10^{-4}	-0.579	-0.625	Sub-critical	Unstable hexagon
5	50	7700	120.596	0.007 25	0.1	5787.7	0.112	-0.276	-0.79×10^{-4}	-0.422	-0.457	Sub-critical	Unstable hexagon

boundary condition is needed to solve the system. Therefore, we have imposed $N(y) = 1$ at $y = 1$. Then the system is solved using the algorithm provided by Cash and Moore.[22] The adjoint problem for $\mathbf{\Theta}$ is also an eigenvalue problem. Then, we solved the system using the same routine[22] by imposing the extra boundary condition $\Theta_2 = 1$ at $y = 1$. The eigenvalue Ra_{τ_c} is the same in both cases. Now, we have found the first-order functions and can calculate ξ_1, ξ_2, and ξ_3 by numerical integration.

Similarly, we have found the second-order functions by numerical solution of four sets of coupled ordinary differential equations using a finite difference technique and Newton iteration method. The solvability condition appears in one of these four sets of equations which require the computed value of ξ_2/ξ_3. Having found the first- and second-order functions, we can find ξ_5 and ξ_6 by numerical integration. The values of k_c, Ra_{τ_c}, and ξ_i for various values of S, H, Le_τ, and Pr_τ are presented in Table II.

The first-order equations do not contain Pr_τ, hence the values of k_c, Ra_{τ_c}, and ξ_3 depend only on S, H, and Le_τ and are independent of Pr_τ. The values of the other ξ_i are more or less independent of Pr_τ. We have solved the system numerically for non-zero k_c by considering the parameter values mentioned in Table I. For $Le_\tau = 1$, we have computed the numerical values of ξ_i for $SH = 0.05, 1, 10$, and 50.

For $SH = 0.05$, $\tilde{\xi}_2 > 0$, $\tilde{\xi}_3 < 0$, and $\tilde{\xi}_5 > \tilde{\xi}_6 > 0$ lead to the first stable transition to down-hexagons from the steady-state [see Fig. 8(c)]. For $SH = 1$, $\tilde{\xi}_2$ becomes negative and $\tilde{\xi}_6 - \tilde{\xi}_5$ becomes positive. So, the first stable transition is to be up-hexagons [Fig. 8(a)]. At $SH = 10$ and 50, $\tilde{\xi}_6 - \tilde{\xi}_5$ becomes again negative, but the first stable transition is still up-hexagons [Fig. 8(b)].

When the value of Le_τ is increased to 5 or more and $SH = 10$ and 50, $\tilde{\xi}_2 < 0$, $\tilde{\xi}_3 < 0$, and $\tilde{\xi}_5 < \tilde{\xi}_6 < 0$. In these cases, both the roll and hexagon branches are sub-critical and unstable [Fig. 8(d)].

VI. JUSTIFICATION OF THE LINEAR ANALYSIS THROUGH FINITE ELEMENT FLOW SIMULATIONS

The governing equation (1) is solved by the finite element method within the Arbitrary Lagrangian Eulerian (ALE)

framework in *Freefem*++ software.[23,24] Taylor-Hood elements known to satisfy Ladyzhenskaya-Babuška-Brezzi (LBB) condition, $([P_2, P_2], P_1)$, are chosen for velocity and pressure in Navier-Stokes equations together with the penalization approach for ensuring divergence-free constraint condition for velocity, while for bacteria density n and oxygen concentration c, P_2 elements are employed for spatial discretization. A characteristic Galerkin formulation based on the material derivative is used in order to stabilize the convection terms. We use a monolithic, fully implicit approach to solve the coupled system of Eq. (1). Let us take the superscript k, denotes the quantity at the time instant $t_k \in [0, T]$, and T is the final time of the numerical simulation. Then, at the time instant t_k, we have $(\mathbf{u}^k, p^k, n^k, c^k)$ on Ω^k in the numerical solution of the system (1), and we will find the unknowns $(\mathbf{u}^{k+1}, p^{k+1}, n^{k+1}, c^{k+1}, \Omega^{k+1})$ at the next time instant t_{k+1}. Therefore, the employed algorithm is of iterative nature.

Mesh Ω^{k+1} is obtained by the physically moving mesh Ω^k so in each time step an additional set of equations has to be solved to obtain grid velocity and iteratively adjust domain at a current time. A domain of interest for the chemotaxis problem is part of the container occupied by fluid. Therefore, if the position of the free-surface is known, the current domain is known as well.

Grid velocity is obtained as a harmonic extension of boundary velocity,

$$-\nabla \cdot \nabla \mathbf{v} = 0, \quad (47)$$

where $\mathbf{v}$ is the grid velocity, $\mathbf{v} = (v_1, v_2)$, subjected to boundary conditions

$$\mathbf{v} = \mathbf{u} \quad \text{on} \quad \Gamma_s \quad (48)$$

and

$$\mathbf{v} \cdot \mathbf{n} = 0 \quad \text{and} \quad \mathbf{v} \cdot \mathbf{t} = \mathbf{u} \cdot \mathbf{t} \quad \text{on} \quad \Gamma_w. \quad (49)$$

In the case of no-slip boundary conditions for Navier-Stokes equations, the boundary condition on the walls for grid velocity is simply $\mathbf{v} = 0$.

We will present few selected direct numerical simulation results of a system of Eq. (1) with the boundary conditions in Eq. (3) prescribed in the rectangular domain of $\Omega = [-5, 5] \times [0, 1]$. The investigated physical domain responds to the case $\epsilon = h/L = 0.1$. The values of the non-dimensional parameters are chosen as follows: $Le_\tau = 1$, $S = 1$, $H = 10$, $Pr_\tau = 7700$,

while Ra_τ = 115, 120.6, and 400. The constant initial data are

$$n(x, y) = \frac{1}{2} 1_{\{y \geq 0.5 + \cos(\frac{2}{5}\pi x)\}} + 1_{\{y < 0.5 + \cos(\frac{2}{5}\pi x)\}},$$

$$c(x, y) = 1, \quad \mathbf{u}(x, y) = 0. \tag{50}$$

The code is run until the numerical solution converges to its steady-state and the result is compared with the analytical solution of Eq. (15b), for which it is easy to verify that $c^* > 0.3$ and thus $r(c) \equiv 1$ (see Fig. 9).

Figure 10 shows the concentration of the bacteria at (a) the initial stage, at time (b) $t = 0.8$, and at (c) $t = 0.2.5$ for Ra_τ = 120.6. It can be seen in the figure that the bacteria have started to consume oxygen and swim toward the higher concentration region which influences the fluid motion. At $t = 0.8$, it can be seen that the domain occupied by the fluid is deformed and that the highest concentration of bacteria is accumulated near the free-surface open to the atmosphere. The chemotaxis-convection process is nearly stabilized at $t = 2.5$. Highest bacteria concentration is near the top where the oxygen concentration is high enough to keep bacteria active which allows them to swim on the free-surface. In the lower

layer, there are some bacteria diluted in the water. This means that the bacteria that ran out of oxygen before they managed to swim to the top (oxygen concentration in the green area is precisely 0.3 which is the border below which bacteria become inactive) and are uniformly distributed due to diffusion effects.

Figures 11 and 12 show the velocity field (magnitude and streamlines) at the beginning of the convection for Ra_τ = 115, 120.6, and 400. When bacteria start consuming oxygen and then start moving toward above to the free-surface due to the lack of oxygen at the below surface, the motion of the bacteria disturbed the static stage of the fluid (initially at rest). We can observe this scenario in the velocity magnitude of the Rayleigh number presented in Figs. 11 and 12: as the Rayleigh number is getting higher, the velocity magnitude increases. When chamber dimensions were chosen, and the total bacteria concentration and the physical parameters of fluid were prescribed, then increasing the Rayleigh number means increasing the bacteria density. Therefore, the obtained results agree with the physical intuition since the higher density of bacteria should disturb the fluid strongly than the lower density bacteria (it needs to swim "harder" to reach the free-surface).
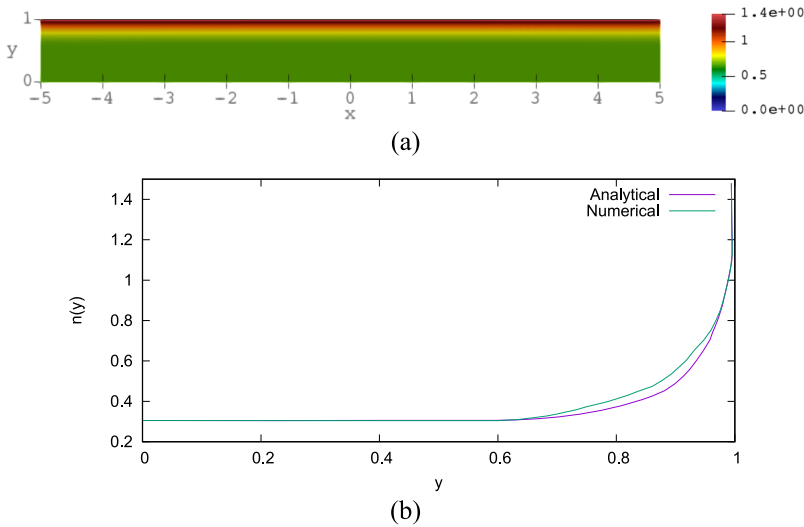

(a)

(b)

FIG. 9. The n-component of (a) the numerical steady-state solution and (b) the agreement of its vertical profile with the analytically calculated one.
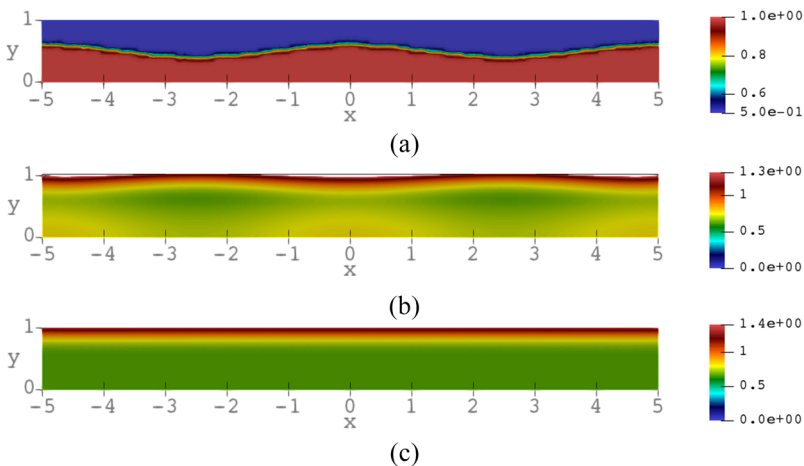

(a)

(b)

(c)

FIG. 10. Bacteria concentration for the case with the Rayleigh number Ra_τ = 120.6. (a) $t = 0.0$. (b) $t = 0.8$. (c) $t = 2.5$.
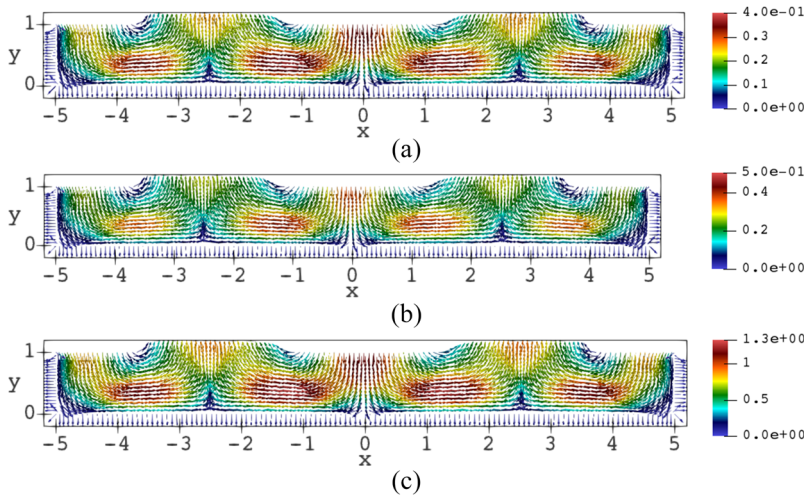
FIG. 11. Velocity field (glyph) at the beginning of the process for Rayleigh numbers: (a) $Ra_\tau = 115$, (b) $Ra_\tau = 120.6$, and (c) $Ra_\tau = 400$.
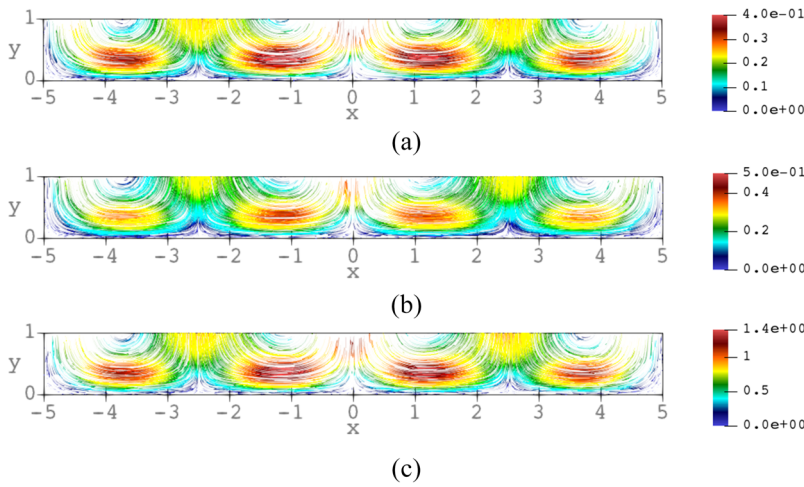

FIG. 12. Velocity field (streamlines) at the beginning of the process for Rayleigh numbers: (a) $Ra_\tau = 115$, (b) $Ra_\tau = 120.6$, and (c) $Ra_\tau = 400$.

Figures 13 and 14 show the velocity field (magnitude and streamlines) at time $t = 2.5$ for $Ra_\tau = 115$, 120.6, and 400. At this time, bacteria that are still active (managed to swim to the free-surface before the oxygen concentration dropped below critical) are concentrated in a thin layer below the free-surface. Since it is denser than the fluid, bacteria need to swim upwards in order to stay in the region with a high oxygen concentration.

Again, the results agree with intuition. The denser bacteria need to swim harder in order to stay on top free-surface and more strongly influence the fluid motion. While in the cases with a lower Rayleigh number, we can observe changes in streamline patterns and lower velocity magnitude, the case with a high Rayleigh number still has fully developed vortex-like streamline patterns and a higher velocity magnitude.
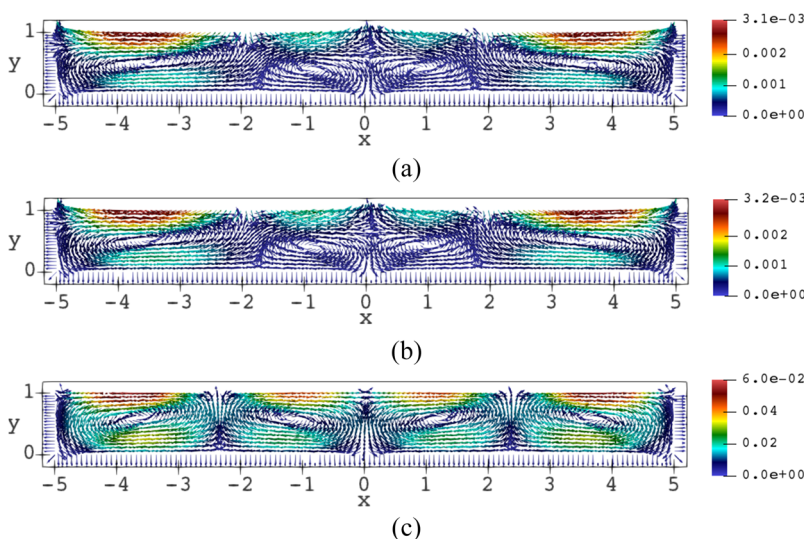

FIG. 13. Velocity field (glyph) at time $t = 2.5$ for Rayleigh numbers: (a) $Ra_\tau = 115$, (b) $Ra_\tau = 120.6$, and (c) $Ra_\tau = 400$.
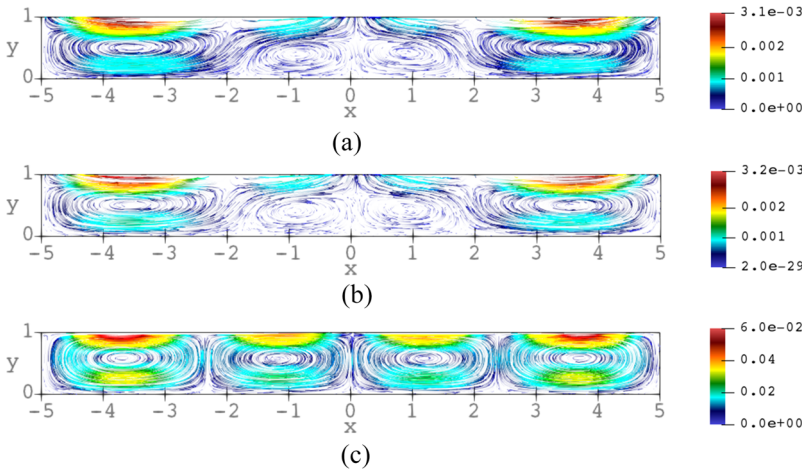
FIG. 14. Velocity field (streamlines) at time $t = 2.5$ for Rayleigh numbers: (a) $Ra_\tau = 115$, (b) $Ra_\tau = 120.6$, and (c) $Ra_\tau = 400$.

VII. CONCLUSIONS

The present study is focused on the exploration of the significant effect on the deformed free-surface of a shallow chamber due to chemotaxis-diffusion-convection of a homogeneous cell system. We have carried out linear stability and weakly nonlinear stability analyses to predict the pattern formed at the onset of instability in the chemotaxis-diffusion-convection system. We have considered the same model described in the work of Deleuze *et al.*[5] for a shallow chamber problem but with a deformed free-surface. We have performed a linear stability analysis by perturbing the steady-state of oxygen and cell concentrations and the free-surface.

It has been found that the increase in Le_τ stabilizes the basic flow because of a uniform distribution of oxygen due to the increment in oxygen diffusion, a smaller gradient of the oxygen concentration, and less rigorously swimming micro-organisms. The length of the shallow chamber also has an impact on the free-surface stability. It is concluded that the wavenumber increases with the length of the chamber as well as the peak of temporal growth. During convection, unstable chemotaxis motion is observed and the cell motion becomes stabilized after reaching the free-surface. The instability generates as the values of H, S, and Le_τ increase, although this effect is reversed as the length of the chamber increases. An increment in the chamber length does not have an impact on cell and oxygen distribution profiles as they are moving vertically. It has been observed that k_c can be either zero or non-zero. If k_c is zero, the system becomes unstable. However, for non-zero k_c, the chemotaxis system stabilizes near the free-surface depending on the values of the parameters H, S, and Le_τ.

The values of H, S, and Le_τ are independently varied, and the corresponding values of Ra_{τ_c} and k_c are determined. The length of the chamber is also varied to study the nature of instability in a shallow chamber. The linear stability of the steady-state depends on the Rayleigh number Ra_τ. If the value of Ra_τ is less than the critical value of Ra_{τ_c}, the steady-state is stable, whereas if Ra_τ is greater than Ra_{τ_c}, the steady-state is unstable. The value of Ra_{τ_c} depends on the wavenumber k of the shallow water wave disturbance. Ra_{τ_c} has its minimum value at the most unstable wavenumber k_c. It is clear from the analytical results of critical Ra_τ and k in comparison with those of Hillesdon and Pedley.[3] The comparison exhibits that our investigated chemotaxis system in shallow chamber reaches the criticality before their system.

The results of the linear stability analysis provide us a useful qualitative perspective of unstable behavior of the cell distribution at the onset of instability, but it is not able to elucidate the initial formation of the bioconvection patterns. Therefore we have carried out a weakly nonlinear stability analysis by expanding the 2D system into 3D (consider z the horizontal coordinate) to investigate the patterns formed at the onset of instability. Ra_τ is the nonlinear control parameter of the system. From our analysis of the steady bifurcating branches, it can be concluded that either roll or hexagonal convection patterns can be stable. It is also useful to mention that either of the up- or down-hexagon can be stable and stable hexagon branches bifurcate supercritically. From bifurcation theory, it was also found that the unstable hexagon branches bifurcate sub-critically for higher values of Le_τ.

Some direct numerical simulation results have been presented in support of our linear stability analyses. The comparison of the steady-state analytical result with the numerical one shows good agreement. Below the critical Rayleigh number, the system is stable. Increasing the Rayleigh number would destabilize the system. It was found that at this position all the bacteria are managed to swim up to the free-surface at a higher oxygen concentration. These bacteria allow themselves to float freely along the free-surface and they are not dense enough yet to fall back to the bottom to form a plume shape. Due to this reason, fully developed vortex-like streamline patterns can be observed at a high Rayleigh number.

We have considered only the shallow chamber case in this research work where all the bacteria have sufficient amount of oxygen concentration to be active. The results may differ in the deep chamber case. It may also be useful to consider a more detailed model for the chemotaxis-diffusion-convection system, which takes the details of the chemotaxis mechanism into account. There is a lack of experiment conducted in this type of problem, but it would be a good scope to explore the study experimentally and numerically as well.

APPENDIX A: SOLUTIONS OF N, $\bar{C}$, AND ψ AT $O(SH/Le_\tau)$ AND $O(SH/Le_\tau)^2$

The solutions of N_1, $\bar{C}_1$, and ψ_1 at the first-order $O(SH/Le_\tau)$ are

$$\psi_1(y) = -i\tilde{k}\varepsilon y^2 \left[\frac{Ra_{\tau_0}}{4!}(y^2 - 4y + 6) \right.$$
$$\left. + \frac{Ra_{\tau_{-1}}}{6!}(2y^4 + 15y^2 - 100y + 180) \right], \quad \text{(A1a)}$$

$$\bar{C}_1(y) = \frac{1}{12}(y^4 + 3y^2 - 4), \quad \text{(A1b)}$$

$$N_1(y) = \frac{1}{2}(2y^2 + 1). \quad \text{(A1c)}$$

At the second-order, the governing equations are

$$\frac{d^4\psi_2}{dy^4} = \frac{\varepsilon\sigma_1}{Pr_\tau}\frac{d^2\psi_1}{dy^2} + \left(\frac{\varepsilon\sigma_2}{Pr_\tau} + 2\varepsilon\tilde{k}^2\right)\frac{d^2\psi_0}{dy^2}$$
$$- i\varepsilon\tilde{k}(Ra_{\tau_1}N_0 + Ra_{\tau_0}N_1 + Ra_{\tau_{-1}}N_2),$$

$$\frac{d^2\bar{C}_2}{dy^2} = \varepsilon\tilde{k}^2\bar{C}_0 + N_2,$$

$$\frac{d^2N_2}{dy^2} = \left(\varepsilon\sigma_2 + \varepsilon^2\tilde{k}^2 + y^2 - \frac{1}{3}\right)N_0 + \left(\frac{y^3}{6} - \frac{y}{6}\right)\frac{dN_0}{dy}$$
$$+ (\varepsilon\sigma_1 + 2)N_1 + y\frac{dN_1}{dy} + y\frac{d\bar{C}_0}{dy} - i\varepsilon\tilde{k}y\psi_0, \quad \text{(A2)}$$

with the boundary conditions

$$\frac{d^3\psi_2(1)}{dy^3} - \frac{\varepsilon\sigma_1}{Pr_\tau}\frac{d\psi_1(1)}{dy} - \left(3\varepsilon^2\tilde{k}^2 + \frac{\varepsilon\sigma_2}{Pr_\tau}\right)\frac{d\psi_0(1)}{dy} = 0,$$

$$\frac{d^2\psi_2(1)}{dy^2} + \varepsilon^2\tilde{k}^2\psi_0(1) = 0,$$

$$\frac{dN_2(1)}{dy} - N_1(1) - \frac{d\bar{C}_1(1)}{dy} - \frac{1}{3}\frac{d\bar{C}_0(1)}{dy} = 0, \quad \bar{C}_2(1) = 0,$$

$$\frac{d\psi_2(0)}{dy} = 0, \quad \psi_2(0) = 0, \quad \frac{dN_2(0)}{dy} = 0, \quad \frac{d\bar{C}_2(0)}{dy} = 0.$$
$$\text{(A3)}$$

The corresponding solutions are

$$\psi_2(y) = \frac{i\tilde{k}^3\varepsilon^3 y^2 Ra_{\tau_{-1}}}{6!}\left[\frac{1}{Pr_\tau}\left(1 - \frac{2Ra_{\tau_{-1}}}{6!}\right)(y^4 - 6y^3 + 15y^2 - 45) - (2y^4 - 12y^3 + 30y^2 \right.$$
$$\left. + 20y - 195) + \frac{6!Ra_{\tau_{-1}}}{11!}(5y^9 - 44y^8 + 165y^7 - 2002y^4 + 16830y^2 - 36685y + 34870)\right]$$
$$- \frac{i\tilde{k}\varepsilon y^2}{4!}\left[\frac{4Ra_{\tau_{-1}}}{7!}(9y^6 + 28y^4 + 630y^2 - 3584y + 6300) + Ra_{\tau_1}(y^2 - 4y + 6)\right.$$
$$\left. + \frac{4Ra_{\tau_0}}{5!}(2y^4 + 15y^2 - 100y - 180)\right], \quad \text{(A4a)}$$

$$\bar{C}_2(y) = \frac{4}{6!}(3y^6 + 5y^4 + 45y^2 - 53) + \frac{\varepsilon\tilde{k}^2}{4!}(y^4 - 6y^2 + 5)$$
$$- \frac{\varepsilon^2\tilde{k}^2 Ra_{\tau_{-1}}}{9!}(5y^9 - 36y^8 + 108y^7 - 546y^4 + 1836y^2 - 1367), \quad \text{(A4b)}$$

$$N_2(y) = \frac{1}{6}(3y^4 + 2y^2 + 3) - \frac{\varepsilon^2\tilde{k}^2 Ra_{\tau_{-1}}}{7!}(5y^7 - 28y^6 + 63y^5 - 91y^2 + 51). \quad \text{(A4c)}$$

APPENDIX B: EXPRESSION OF ξ_i

The expressions for the ξ_i appearing in the solvability conditions and evolution equations are presented here. The functions J_i, G_i, and E_i in ξ_5 and ξ_6 are the solutions to the second-order differential equations,

$$\xi_1 = \int_0^1 \frac{1}{Pr_\tau}\Theta_1(V'' - k^2 V') + \Theta_2 N + \frac{1}{Le_\tau}\Theta_3 C\, dy, \quad \text{(B1a)}$$

$$\xi_2 = \int_0^1 \left[\frac{\Theta_1}{Pr_\tau}\left(V'V'' + \frac{1}{2}VV''' - \frac{3}{2}k^2 VV'\right) + \Theta_2\left(VN' + \frac{1}{2}V'N - \frac{1}{2}Sk^2 CN\right.\right.$$
$$\left.\left. + SN'C' + SNC''\right) + \frac{\Theta_3}{Le_\tau}\left(VC' + \frac{1}{2}V'C'\right)\right]dy + (\Theta_2 SNC')|_{y=0}, \quad \text{(B1b)}$$

$$\xi_3 = \int_0^1 \Theta_1 k^2 N dy, \tag{B1c}$$

$$\begin{aligned}
\xi_5 = \int_0^1 \bigg[& \frac{\Theta_1}{Pr_\tau} k^2 \bigg(-\frac{3}{4} k^2 VE_6' - \frac{9}{4} k^2 VE_7' - \frac{3}{4} k^2 V'E_6 - \frac{15}{4} k^2 V'E_7' + \frac{1}{2} V'E_6'' + \frac{3}{2} V'E_7'' + \frac{1}{2} V''E_6' + \frac{1}{4} VE_6''' + \frac{3}{4} VE_7''' \\
& + \frac{1}{4} V'''E_6 - \frac{3}{4} V'''E_7 \bigg) + \Theta_2 \bigg(\frac{S}{2} C'J_6' + \frac{S}{2} C''J_6 - \frac{S}{4} k^2 CJ_6 + \frac{S}{2} C'J_7' + \frac{S}{2} C''J_7 + \frac{S}{4} k^2 CJ_7 + SC'J_4' + SC''J_4 - Sk^2 CJ_4 \\
& - \frac{S}{4} k^2 NG_6 - \frac{3}{4} Sk^2 NG_7 + \frac{1}{2} k^2 NE_6' + \frac{3}{4} k^2 NE_7' + \frac{1}{2} k^2 N'E_6 + \frac{3}{2} k^2 N'E_7 + VJ_4' + \frac{1}{4} VJ_6' + \frac{1}{4} VJ_7' + \frac{1}{4} V'J_6 + \frac{3}{4} V'J_7 + SN'G_4' \\
& + \frac{S}{2} N'G_6' + \frac{S}{2} N'G_7' + SNG_4'' + \frac{S}{2} NG_6'' + \frac{S}{2} NG_7'' \bigg) + \frac{\Theta_3}{Le_\tau} \bigg(\frac{1}{2} k^2 C'E_6 + \frac{3}{2} k^2 C'E_7 + \frac{1}{4} k^2 CE_6' + \frac{3}{4} k^2 CE_7' + VG_4' + \frac{1}{2} VG_6' \\
& + \frac{1}{2} VG_7' + \frac{1}{4} V'G_6 + \frac{3}{4} V'G_7 \bigg) \bigg] dy + \bigg[\Theta_2 S \bigg(C'J_4 + \frac{1}{2} C'J_6 + \frac{1}{2} C'J_7 + NG_4' + \frac{1}{2} NG_6' + \frac{1}{2} NG_7' \bigg) \bigg] \bigg|_{y=0},
\end{aligned} \tag{B1d}$$

$$\begin{aligned}
\xi_6 = \int_0^1 \bigg[& \frac{\Theta_1}{Pr_\tau} k^2 \bigg(-3k^2 VE_8' - 6k^2 V'E_8 + 2V'E_8'' - V''E_8' + VE_8''' - 2V'''E_8 \bigg) \\
& + \Theta_2 \bigg(SJ_4'C' + SJ_4 C'' - Sk^2 CJ_4 + \frac{S}{2} J_8'C' + \frac{S}{2} J_8 C'' + \frac{S}{2} k^2 CJ_8 + SN'G_4' \\
& + SNG_4'' + \frac{S}{2} N'G_8' + \frac{S}{2} NG_8'' - Sk^2 NG_8 + VJ_4' + \frac{1}{2} VJ_8' + V'J_8 + k^2 NE_8' \\
& + 2k^2 N'E_8 \bigg) + \frac{\Theta_3}{Le_\tau} \bigg(2k^2 C'E_8 + k^2 CE_8' + VG_4' + \frac{1}{2} VG_8' + V'G_8 \bigg) \bigg] dy \\
& + \bigg[\Theta_2 S \bigg(C'J_4 + \frac{1}{2} C'J_8 + NG_4' + \frac{1}{2} NG_8' \bigg) \bigg] \bigg|_{y=0}.
\end{aligned} \tag{B1e}$$

[1] N. A. Hill and T. J. Pedley, "Bioconvection," Fluid Dyn. Res. **37**, 1 (2005).

[2] A. J. Hillesdon, T. J. Pedley, and J. O. Kessler, "The development of concentration gradients in a suspension of chemotactic bacteria," Bull. Math. Biol. **57**, 299 (1995), available at https://www.sciencedirect.com/science/article/pii/009282409400038E.

[3] A. J. Hillesdon and T. J. Pedley, "Bioconvection in suspensions of oxytactic bacteria: Linear theory," J. Fluid Mech. **324**, 223 (1996).

[4] A. Chertock, K. Fellner, A. Kurganov, A. Lorz, and P. A. Markowich, "Sinking, merging and stationary plumes in a coupled chemotaxis-fluid model: a high-resolution numerical approach," J. Fluid Mech. **694**, 155 (2012).

[5] Y. Deleuze, C. Y. Chiang, M. Thiriet, and T. W. H. Sheu, "Numerical study of plume patterns in a chemotaxis-diffusion-convection coupling system," Comput. Fluids **126**, 58 (2016).

[6] E. F. Keller and L. A. Segel, "Model for chemotaxis," J. Theor. Biol. **30**, 225 (1971).

[7] A. A. Avramenko and A. V. Kuznetsov, "Bio-thermal convection caused by combined effects of swimming of oxytactic bacteria and inclined temperature gradient in a shallow fluid layer," Int. J. Numer. Methods Heat Fluid Flow **20**, 157 (2010).

[8] A. V. Kuznetsov, "Investigation of the onset of thermo-bioconvection in a suspension of oxytactic microorganisms in a shallow fluid layer heated from below," Theor. Comput. Fluid Dyn. **19**, 287 (2005).

[9] A. J. Hillesdon, "Pattern formation in a suspension of swimming bacteria," Ph.D. thesis, University of Leeds, 1994.

[10] N. A. Hill, T. J. Pedley, and J. O. Kessler, "Growth of bioconvection patterns in a suspension of gyrotactic micro-organisms in a layer of finite depth," J. Fluid Mech. **208**, 509 (1989).

[11] A. M. Metcalfe and T. J. Pedley, "Falling plumes in bacterial bioconvection," J. Fluid Mech. **445**, 121 (2001).

[12] R. Kowalczyk, A. Gamba, and L. Preziosi, "On the stability of homogeneous solutions to some aggregation models," Discrete Contin. Dyn. Syst.: Ser. B **4**, 203 (2004).

[13] A. M. Metcalfe and T. J. Pedley, "Bacterial bioconvection: Weakly nonlinear theory for pattern selection," J. Fluid Mech. **370**, 249 (1998).

[14] M. Ma, M. Gao, C. Tong, and Y. Han, "Chemotaxis-driven pattern formation for a reaction-diffusion-chemotaxis model with volume-filling effect," Comput. Math. Appl. **72**, 1320 (2016).

[15] I. Tuval, L. Cisneros, C. Dombrowski, C. W. Wolgemuth, J. O. Kessler, and R. E. Goldstein, "Bacterial swimming and oxygen transport near contact lines," Proc. Natl. Acad. Sci. U. S. A. **102**, 2277 (2005).

[16] R. Duan, A. Lorz, and P. Markowich, "Global solutions to the coupled chemotaxis-fluid equations," Commun. Partial Differ. Equations **35**, 1635 (2010).

[17] J. G. Liu and A. Lorz, "A coupled chemotaxis-fluid model: Global existence," Ann. Inst. Henri Poincare (C) Nonlinear Anal. **28**, 643 (2011).

[18] S. Chandrasekhar, *Hydrodynamic and Hydromagnetic Stability* (Oxford University Press, 1961).

[19] M. Bestehorn, in *Encyclopedia of Complexity and System Science*, edited by R. A. Meyers (Springer, Berlin, 2009).

[20] E. Buzano and M. Golubitsky, "Bifurcation on the hexagonal lattice and the planar Bénard problem," Philos. Trans. R. Soc., A **308**, 617 (1983).

[21] M. Golubitsky, J. W. Swift, and E. Knobloch, "Symmetries and pattern selection in Rayleigh- Bénard convection," Phys. D **10**, 249 (1984).

[22] J. R. Cash and D. R. Moore, "A high order method for the numerical solution of two-point boundary value problems," BIT **20**, 44 (1980).

[23] A. Decoene and B. Maury, "Moving meshes with FreeFem++," J. Numer. Math. **20**, 195 (2013).

[24] F. Hecht, "New development in FreeFem++," J. Numer. Math. **20**, 251 (2013).